

**Texas A&M University
Mechanical Engineering Department
Turbomachinery Laboratory**

Test Results for Load-On-Pad and Load-Between-Pad Hybrid Flexure Pivot Tilting Pad Gas Bearings

Research Progress Report to the Turbomachinery Laboratory

TL-B&C-1-06

by

Luis San Andrés
Mast-Childs Professor
Principal Investigator

Keun Ryu
Research Assistant

June 2006

Test Results for Load-On-Pad and Load-Between-Pad Hybrid Flexure Pivot Tilting Pad Gas Bearings

Executive Summary

Gas film bearings offer unique advantages enabling successful deployment of high-speed micro-turbomachinery. Current applications encompass micro power generators, air cycle machines and turbo expanders. Mechanically complex gas foil bearings are in use; however, their excessive cost and lack of calibrated predictive tools deter their application to mass-produced oil-free turbochargers, for example.

Rotordynamic measurements on a test rotor, 0.825 kg and 28.6 mm diameter, supported on hybrid (hydrostatic/hydrodynamic) flexure pivot tilting pad gas bearings are performed for various imbalances, increasing supply pressures, and under load-on-pad (LOP) and load-between-pad (LBP) configurations. From prior testing, the bearing pads have uneven wear and thus dissimilar clearances which affect the dynamics of the rotor-bearing system. In coast down rotor responses from 50 krpm, the rotor traverses critical speeds corresponding to rigid body modes. There are no noticeable differences in rotor response for the LOP and LBP configurations due to the light-weight rotor, i.e. small static load acting on each bearing. External pressurization into the bearings increases their direct stiffnesses and reduces their damping, while raising the system critical speed and evidencing a reduction in viscous damping ratios. External pressurization into the bearings determines large times for rotor deceleration, thus demonstrating the little viscous drag typical of gas bearings. Rotor deceleration tests with manually controlled supply pressures eliminate the passage through critical speeds, thus showing a path for rotordynamic performance without large amplitude motions over extended regions of shaft speed. Predicted bearing force coefficients for the LOP and LBP cases are nearly identical within the test speed range. The rotordynamic analysis shows critical speeds and peak amplitudes of motion agreeing very well with the measurements. The synchronous rotor responses for increasing imbalances demonstrate the test system linearity. Pressurized flexure pivot gas bearings are mechanically complex and costly, but their superior stability and predictable performance can further their implementation in high performance oil-free microturbomachinery.

TABLE OF CONTENTS

	<u>Page</u>
Executive Summary	ii
List of Tables	iv
List of Figures	iv
Nomenclature	vii
Introduction	1
Review of Relevant Literature	3
Experimental Facility	6
Experimental Procedure	11
Experimental Results	13
Baseline rotor responses	13
Comparison of rotor responses for increasing supply pressures into the gas bearings	18
Rotor responses with added imbalance masses	20
Control of supply pressure to eliminate passage through a critical speed	22
Coast down rotor speed and type of drag	24
Predictions of rotordynamic response and comparison to test results	27
Mass flow rate	27
Rotor model: Free-free mode natural frequencies and shapes	28
Damped natural frequencies and damping ratios	30
Comparison between predictions and tests of imbalance response	31
Conclusions	33
References	35
Appendix A. Predicted bearing stiffness and damping force coefficients	37

LIST OF TABLES

	Page	
1	Main parameters of test rig and flexure pivot bearings	5
2	List of sensors gains	6
3	Imbalance mass magnitudes and locations	7
4	Assumed clearance and preload for prediction of dynamic force response of test bearings	10
5	Comparison of measured and predicted free-free mode natural frequencies	11

LIST OF FIGURES

	<u>Page</u>	
1	Schematic cross section view of gas bearing test rig	15
2	Schematic view of rotor	15
3	Photograph and dimensions of flexure pivot tilting pad hydrostatic bearing	15
4	Estimated radial clearances and axial shape of pads in test bearings	16
5	Rotation of rig for experiments with load-between-pad condition on test bearings	17
6	Bearing configurations for Load-on-pad (LOP) and Load-between-pad (LBP) conditions	17
7	Locations of imbalance masses at end faces of rotor	18
8	Amplitudes of rotor synchronous response versus speed. Baseline imbalance, LOP condition, 5.08 bar feed pressure, slow roll compensation at 4000 rpm	19
9	Phase difference (left – right) of recorded imbalance responses versus speed. Baseline imbalance, LOP condition, 5.08 bar feed pressure, slow roll compensation at 4000 rpm	19
10	Amplitude ratio (left / right) of recorded imbalance responses versus speed. Baseline imbalance, LOP condition, 5.08 bar feed pressure, slow roll compensation at 4000 rpm	20
11	Amplitudes of rotor synchronous response versus speed. Baseline imbalance, LBP condition, 5.08 bar feed pressure, slow roll compensation at 4000 rpm	20
12	Waterfall of baseline rotor motions for test with 5.08 bar feed pressure Left bearing, 45°CW plane, LBP condition	21
13	Synchronous speed rotor orbits for baseline condition, Load on Pad configuration, 5.08 bar feed pressure. Slow roll compensation at 4000 rpm	22
14	Synchronous speed rotor orbits for baseline condition, Load on Pad configuration, 5.08 bar feed pressure. Slow roll compensation at 4000 rpm	22
15	1X rotor orbits for baseline condition, Load on Pad and Load Between Pads configurations, 5.08 bar feed pressure, 45 krpm shaft speed	22
16	Effect of increasing supply pressure on test rotor synchronous response. LOP condition, Baseline imbalance, slow roll compensation at 4000 rpm. Measurement on side of right bearing (vertical direction)	23
17	Effect of increasing supply pressure on test rotor synchronous response. LBP condition, Baseline imbalance, slow roll compensation at 4000 rpm. Measurement on side of right bearing (45° CW from vertical)	23

18	Amplitudes of rotor synchronous response versus speed. Imbalance U(B ₂): 0.034 gram , LOP condition, 5.08 bar feed pressure, slow roll compensation at 4000 rpm	24
19	Effect of increasing imbalance mass on peak amplitude of rotor synchronous response. LOP condition. Displacements at left bearing, vertical direction (LV). Baseline response subtracted	24
20	Comparison of measured peak amplitudes of rotor motion for various imbalances and supply pressure conditions. LOP configuration. Displacement at left bearing, vertical direction (LV). Baseline response subtracted.	25
21	Manual changes in supply pressure as rotor speed coasts down	26
22	Amplitudes of rotor synchronous response versus speed for controlled feed pressures. LOP condition, Baseline imbalance, slow roll compensation at 4,000 rpm. Measurements at right bearing side, vertical direction (RV)	26
23	Effect of supply pressure on length of coast-down rotor deceleration. (a) LOP and (b) LBP configurations. Baseline imbalance	27
24	Comparison of rotor speed coast-down curves versus time for various imbalance conditions (baseline, U(A ₃) and U(B ₃)) at 3.72 bar absolute feed pressure (LOP configuration)	28
25	Measured and predicted mass flow rates versus supply pressure for test bearings (LOP configuration)	28
26	Structural model of test rotor	29
27	Measured and predicted free-free mode shapes for test rotor	29
28	Damped natural frequency map of test rotor-bearing system. 5.08 bar feed pressure. LOP configuration	30
29	Predicted damping ratios versus rotor speed. 5.08 bar feed pressure. LOP configuration	30
30	Mode shapes of rotor at critical speeds. 5.08 bar feed gas pressure. LOP configuration	31
31	Predicted and measured imbalance response for three mass imbalance conditions, U(B ₁)=0.44 μm, U(B ₂)=0.49 μm, U(B ₃)=0.58 μm.. Tests at 5.08 bar feed pressure (LOP configuration). Displacements at left bearing, vertical direction (LV). Baseline response subtracted.	31
32	Predicted and measured normalized imbalance responses, U(B ₃)= 0.58 μm and U(B ₁)=0.44 μm. Tests at 5.08 bar feed pressure (LOP configuration). Displacements at left bearing, vertical direction (LV). Baseline response subtracted.	32
A.1	Predicted static journal eccentricity (e/C) for increasing feed pressures. LOP and LBP configurations. Static load $W=4.04$ N	38
A.2	Predicted attitude angle for increasing feed pressures. LOP and LBP configuration. Static load $W=4.04$ N	39
A.3	Predicted synchronous direct stiffnesses vs. speed. Left and right bearings. LOP configuration. Supply pressures (a) 5.08 bar, (b) 3.72 bar, (c) no feed pressure	40
A.4	Predicted synchronous direct damping coefficients vs. speed. Left and right bearings. LOP configuration. Supply pressures (a) 5.08 bar, (b) 3.72 bar, (c) no feed pressure	41
A.5	Predicted synchronous cross stiffnesses vs. speed. Left and right bearings. LOP configuration. Supply pressures (a) 5.08 bar, (b) 3.72 bar, (c) no feed	42

	pressure	
A.6	Predicted synchronous cross damping coefficients vs. speed. Left and right bearings. LOP configuration. Supply pressures (a) 5.08 bar, (b) 3.72 bar, (c) no feed pressure	43
A.7	Comparison of direct and cross-coupled stiffnesses for LOP and LBP configurations. Right bearing without feed pressure. Synchronous speed coefficients	44
A.8	Comparison of direct and cross-coupled damping coefficients for LOP and LBP configurations. Right bearing without feed pressure. Synchronous speed coefficients	45

NOMENCLATURE

C_p	Bearing clearance [m]
d_o	Feed orifice diameter [m]
D_j	Rotor Diameter [m]
e	Journal eccentricity [m]
I_p	Pad mass moment of Inertia [kg-m ²]
$K_{\delta\delta}$	Web rotational stiffness [Nm/rad]
L_r	Rotor length
L	Bearing axial length [mm]
m_i	Calibrated imbalance mass [g]
m_p	Pad mass [kg]
M	Rotor mass [kg]
M_l	Half of rotor mass [kg]
M_{left}	Imbalance mass of left rotor [kg]
M_{right}	Imbalance mass of right rotor [kg]
N	Rotor speed [rev/min]
R_p	Pad radius [m]
R_j	Rotor radius [m]
R'	Radial location of imbalance mass [m]
u	Mass imbalance displacement [m]
W	Rotor weight [lb]
ϕ_{left}	Phase angle of imbalance mass location for left rotor [rad]
ϕ_{right}	Phase angle of imbalance mass location for left rotor [rad]
Ω	Angular frequency [Hz]

Introduction

Microturbomachinery (MTM) includes turbochargers, auxiliary power units for aircrafts and gas turbine power engines (< 400kW). MTM typically operates at high speeds and delivers reliable power in compact units of low weight. High performance microturbomachinery implements gas bearings to improve mechanical efficiency while reducing overall system weight and eliminating complex mineral oil lubrication systems.

The inherent advantages of gas bearings include very low friction (reduced drag power losses) with less heat generation, as well as operation at extreme temperatures, cold or hot. However, gas bearings have low hydrodynamic load-carrying capacity since the material viscosity of gases is quite small. This limitation also results in very low damping force coefficients, not large enough to dissipate effectively vibrational energy and to reduce amplitudes of motion while traversing critical speeds, for example. Gas bearings operate most effectively at high surface speeds where rotor lift-off is ensured. At low surface speeds, while at rotor start-up or shutdown, gas bearings are not able to generate large enough hydrodynamic pressures supporting applied (static or dynamic) loads; and thus, intermittent or sustained operation with contact of the rotor within its bearings is unavoidable. This operating condition increases dramatically the friction and drag, while accelerating the wear (and damage) of the surfaces in contact. Transmitted forces to the machine casing could be quite large; and at times; potentially catastrophic dry-friction whirl and whip instabilities could occur. Thin solid lubricants are typically coated on the bearings' surfaces and the rotor to reduce friction and wear and ensure rotor lift-off at relatively low surface speeds. At present, (hard and soft) coatings are engineered from various materials and deposition processes to perform the intended function, in particular when operation demands extreme changes in temperature, as is the case with gas turbine engines and turbochargers, for example.

Gas bearings integrating external pressurization (hydrostatic bearings) offer a simple way to avoid the issues of contact and wear during start up and shut down. While the rotor rests on its bearings (not spinning), the external pressure lifts the rotor thus eliminating the likeliness of contact while the machine starts up, i.e. rotor spinning and accelerating towards its intended operating condition. Hydraulic pressure jacking is common in heavy weight large rotating machinery supported on oil lubricated bearings, for example. The external pressure source represents an added cost and complexity, yet its benefits are immediately recognizable. Within the framework of MTM applications, the pressurized gas (air typically) could be readily available in small canisters. In operation of a turbocharger, for example, gas

bleed-off from the compressor can readily replenish the pressurized gas spent during start-up. Micro-gas turbines are already implementing this concept. [1]

Tilting pad bearings are widely applied in high performance TM because of their proven stability characteristics based on no cross-coupled stiffness coefficients, thus free of rotordynamic instability. Flexure pivot tilting pad bearings were introduced to provide many of the advantageous rotordynamic characteristics of tilting pad bearings with a single-piece mechanical component fabricated with the electric discharge machining (EDM) process.

The main objective of the research at TAMU is to advance the technology of gas bearings for oil-free micro-turbomachinery by performing measurements of rotordynamic response on a test rotor supported on gas bearings and advancing predictive computational models benchmarked by the test data. San Andrés and co-workers [2-5] present comprehensive rotordynamic experiments conducted on a small rotor supported on three lobed hybrid gas bearings, flexure pivot tilting pad hydrostatic bearings, and Rayleigh step gas bearings. The Rayleigh step gas bearings are the most unstable and unreliable bearing configuration, while flexure tilting pad gas bearings show a superior dynamic performance than the other bearings.

The current work continues earlier research [4] and presents further rotordynamic measurements of a test rotor supported on the flexure pivot tilting pad gas hydrostatic bearings. The tests are conducted with the bearings under load-on-pad (LOP) and load-between-pad (LBP) configurations. Rotor speed coast-down tests to calibrated imbalance masses are performed for various feed gas pressures. Predictions from computational programs for gas bearing performance and rotordynamic response show excellent agreement with the experimental results.

Review of Relevant Literature

Gas bearings are widely used as support elements in high speed small rotating machinery due to their distinct advantages compared with oil-lubricated bearings. Gas bearings eliminate complex oil lubrication and sealing systems, and reduce friction, heat generation and power losses. These advantages have led to commercial applications in MTM (output power below 400kW) with distinctive advantages including compact size, light weight and low energy costs. MTM typically operates at high rotational speed and extreme temperatures.

Gas bearings, however, have relatively much lower load-carrying capacity, direct stiffness and damping, than oil-lubricated bearings [6]. The static and dynamic performance characteristics of gas bearings can be improved by reducing the operating clearances or by increasing the system rotational speed [7]. Minute bearing clearances demand of a manufacturing process with strict tolerances, thus increasing their fabrication cost, installation and maintenance.

The research and development of gas bearings experienced a rapid growth between 1950 and 1970. Before 1960, the applications of gas bearings were limited to gyroscopes for inertial navigation and gas circulators in nuclear reactors. The research on gas bearings concerning these applications was initiated in the UK at the Admiralty Compass Observatory and AERE Harwell in the late 1950s. After this period, gas bearings have been applied successfully in spindle machines, dental hand tools and medical and scientific instruments [8]. Gross [9] and Fuller [10] offer detailed literature reviews on gas bearings prior to 1969.

In the early 1960s, Gunter et al. [11, 12] researched tilting pad gas bearings because of their good stability characteristics, load-carrying capacity and self-align ability. The authors also advance predictive models for load capacity and comparisons to test results, and determine the optimum pivot location. Lund [13] introduces the pad assembly method to predict stiffness and damping coefficients of tilting pad journal bearings, and considers the effects of pad inertia, bearing slenderness ratio, static load direction, and pad preload. Pitts [14] presents a design method for disposition of the pivot in tilting pad gas bearings and provides design charts for bearings with increasing number of pads and various pivot positions. Lund [15] provides a method to predict stiffness and damping force coefficients of gas bearings based on the perturbation of the Reynolds equation from small amplitude journal motions about an equilibrium position.

Excessive drag during start-up/shut-down and limited load-carrying capacity of hydrodynamic gas bearings can be resolved by introducing external pressurization. Hydrostatic effects lifting a rotor reduce wear of bearing surfaces at start-up/shut-down,

provide additional stiffness, and also reduce the operating eccentricity of the bearings. Shapiro [16] discusses the effect of pressurized gas to increase the load-carrying capacity of gas bearings. Wilde and San Andrés [2, 3] conduct comprehensive rotordynamic experiments on a small rotor supported on three-lobed hybrid gas bearings. The bearings are simple and inexpensive, and when externally pressurized show adequate dynamic force characteristics, low friction and wear during transient startup and enhanced rotordynamic stability for high speed oil-free turbomachinery.

Tilting pad bearings offer inherent dynamic stability at the expense of mechanical complexity. These bearings comprise of several pads able to pivot or tilt to accommodate rotor movements, thus reducing or eliminating destabilizing cross-coupled stiffnesses. Flexure pivot tilting pad bearings, machined as a single piece using wire EDM, offer the same advantages as tilting pad bearings. This bearing type also eliminates pivot wear and contact stresses, pad flutter, and minimizes manufacturing and assembly tolerance stack-up. Zeidan [17], Armentrout et al [18], and Chen [19] discuss practical design issues in flexure pivot tilting pad bearings. Armentrout et al [18] calculate flexure pivot tilting pad bearing stiffness and damping coefficients as a function of the pad flexure rotational stiffness, and also present a rotordynamic analysis for a high-speed turbocompressor implementing these bearings. As the flexural stiffness increases, the performance of flexure pivot tilting pad bearings varies from that of an (ideal) tilting pad bearing rigid bearing to that of a fixed-geometry bearing [19].

De Choudhury et al [20], Chen et al [21], and Kepple et al [22] report relevant field experiences with flexure pivot bearings. De Choudhury et al [20] present imbalance responses of a two stage compressor rotor supported on flexure pivot tilting pad bearings. These bearings determine lower temperature operation and less drag power losses when compared to identical size five-pad tilting pad journal bearings. Chen et al [21] demonstrate that the vibration of a compressor rotor decreases with flexible pivot tilting pad bearings as compared to conventional tilting pad bearings for unusual operation under surge conditions. Kepple et al [22] describe field applications of TM rotors becoming stable when implementing flexure pivot tilting pad bearings; opposite effects being observed with spherical pivot tilting pad bearings.

For use in oil-free TM, Zhu and San Andrés [4] demonstrate the stable performance of a high speed rotor supported on hybrid (hydrostatic and hydrodynamic) flexure pivot tilting pad bearings. Measurements of rotor coast down responses for increasing levels of external pressurization into the bearings show that the bearing stiffness and system critical speed

increase as the feed pressure increases. However, the damping ratio of the rotor-bearing system decreases. Tests without supply pressure show the rotor becomes unstable at ~81 krpm with a whirl frequency ratio of 20%. With external pressurization, the rotor-bearing system is stable to the top speed, 100 krpm, of the drive motor. Zhu and San Andrés [5] also perform similar experiments with a rotor supported on Rayleigh step gas bearings. Severe instabilities arise at nearly fixed whirl frequencies (system natural frequency). The test Rayleigh step gas bearings exhibit a much reduced stable operation range, up to ~20 krpm.

Gas foil bearings, in use in commercial micro turbomachinery, offer high temperature operation with tolerance to large rotor motions (rubbing and misalignment) and a load capacity exceeding that of rigid surface gas bearings. Kim and San Andrés [23] present an efficient computational tool for prediction of the static and dynamic force performance of foil bearings. San Andrés et al. [24] measure the rotordynamic performance of a test rotor supported on foil bearings and find severe subsynchronous whirl motions forced by increasing imbalances. The design tools and experimental results complement the development of oil-free TM with high efficiency. References [23, 24] include relevant literature reviews on gas foil bearings and their state of art.

Experimental Facility

Figure 1 shows the schematic cross sectional view of the gas bearing test rig with a steel main body integrating a brushless DC motor armature (max. speed 99 krpm). The test rotor, shown in Figure 2, is supported on two flexure pivot hydrostatic bearings, denoted as left and right, respectively. Pins with a spring loaded elastomer head hold the rotor axially. Alignment bolts, position the test bearings, shown in Figure 3, within their housings. Piezoelectric load cells are installed between each bolt and bearing outer surface. Side caps and o-rings push on the bearing sides to form a circular feed groove for external pressurization into the bearings.

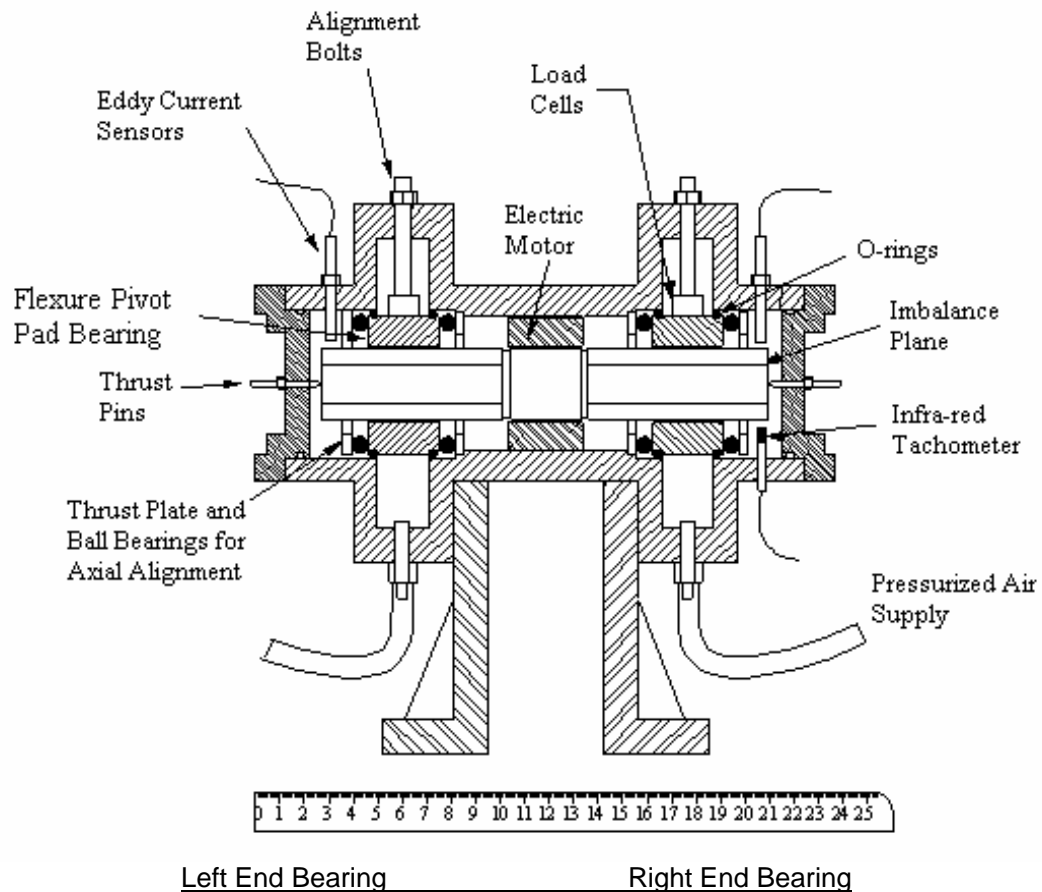


Fig. 1 Schematic cross section view of gas bearing test rig (Unit: cm)

Figure 2 displays the rotor, 0.825 kg in mass, comprised of a steel shaft, 15mm in diameter and 190mm in length, onto which two cylindrical sleeves are press-fit. The rotor has a diameter of 28.55 mm. The rotor at the bearing locations is hard-chrome coated (thickness 0.010 in \pm 0.001 inch). On each rotor end face, eight holes, 1 mm in diameter, are spaced

equally. Imbalance masses are placed in these holes for imbalance response measurements. Table 1 lists the dimensions of the test rotor and its bearings.

Figure 3 depicts a test flexure pivot tilting pad hybrid bearing. Each bearing, made of bronze, has four arcuate 72° pads connected to the housing through a thin structural web. Four radial holes are machined directly through the flexural webs and serve to pressurize each pad. A coating of Permalon® ($10 \pm 1 \mu\text{m}$ thick) was applied on the pads surfaces to reduce friction upon rotor start-up and shutdown. The surface of each pad was finished with 600 grit ultra fine grade sandpaper.

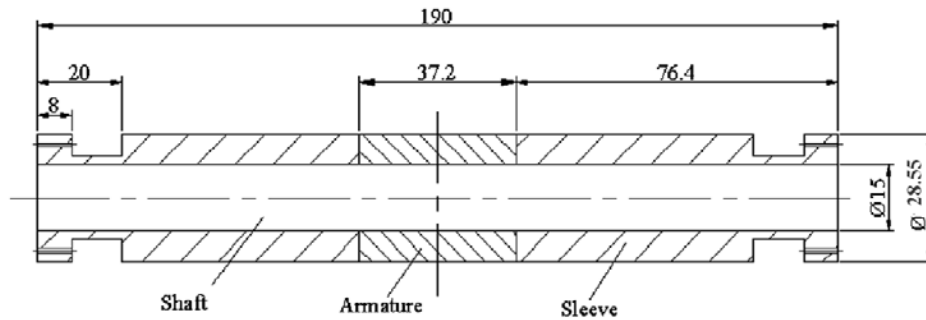


Fig. 2 Schematic view of rotor (units: mm)

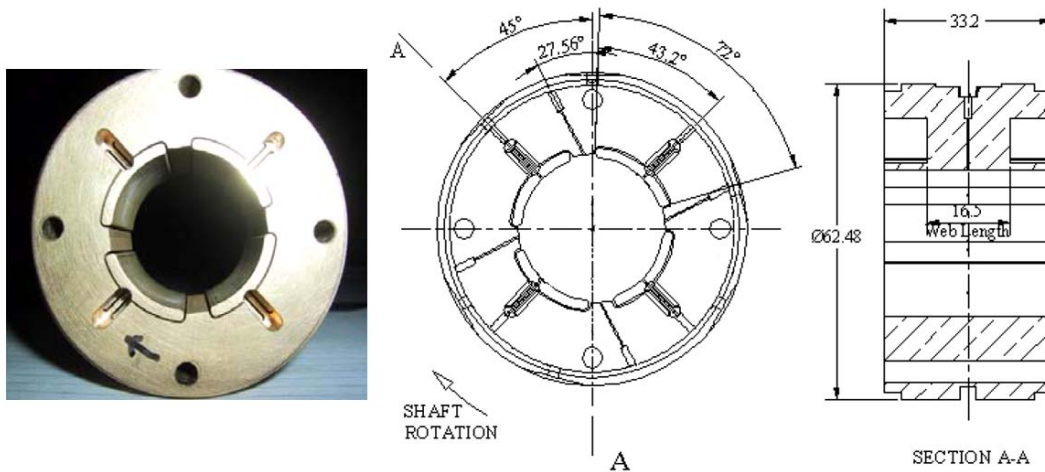


Fig. 3 Photograph and dimensions of flexure pivot tilting pad hydrostatic bearing (units: mm)

Prior extensive testing with the bearings [4] left the pad surfaces with a number of scratches and uneven wear. The present condition of the bearings, even after application of the coating and hand polishing, shows quite dissimilar clearances on each pad, both along their circumference and axial position. The bearing clearance is estimated by subtracting the

rotor diameter from the bearing diameter. The pad curvature is generally established prior to initial machining, and the pad clearance is equal to the machined pad bore diameter minus the rotor diameter. Presently, the estimated radial clearances vary from 20~60 μm for the left bearing and 20~40 μm for the right bearing.

Table 1. Main parameters of test rig and flexure pivot bearings

	<i>Parameter</i>	<i>Value</i>	<i>Unit</i>
Rotor	Mass, M	0.825	kg
	Diameter, D_j	28.55 ± 0.001	mm
	Length, L_r	190	mm
Bearing 4 pads	Axial Length, L	33.2	mm
	Pivot offset	60%	
	Arc length	72°	
	Pad mass, m_p	10.85	gram
	Pad mass moment of Inertia, I_p	0.253	gram-mm ²
	Web rotational stiffness, $K_{\delta\delta}$	20	N-m/rad
	Feed orifice diameter	0.62	mm

Figure 4 depicts the estimated bearing clearances along the axial length of each bearing. Graphs depicting the approximate curved shape of the pads aid to visualize the bearings' current condition. Note that the left bearing has a much larger clearance distribution than the right bearing. This geometrical condition will have a profound impact on the actual static and dynamic performance characteristics of the rotor-bearing system since one bearing will show larger direct stiffnesses than the other; thus affecting the critical speeds locations and imbalance response of the rotor.

Pairs of eddy current sensors, orthogonally positioned and facing the rotor ends, measure the rotor motions along the X -(vertical) and Y -(horizontal) planes. Table 2 lists the sensitivities of the eddy current sensors and load cells. An infrared tachometer serves as a keyphasor signal for data acquisition. A Bentley Nevada ADRE® data acquisition system and Labview® DAQ system acquire and save the data during coast-down response tests.

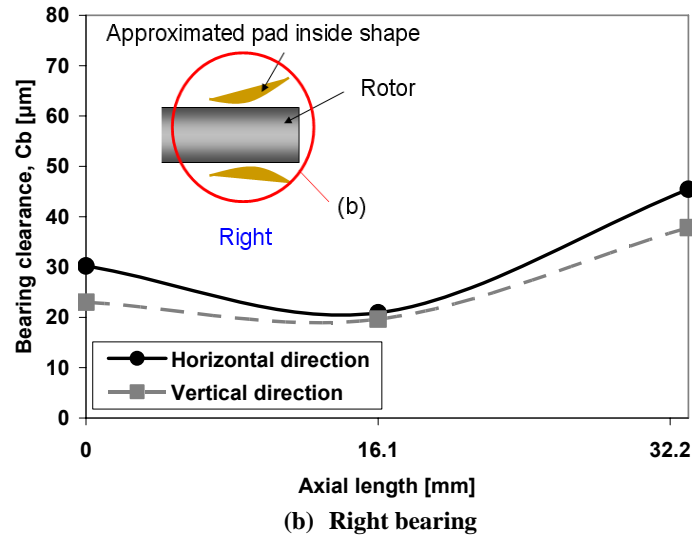
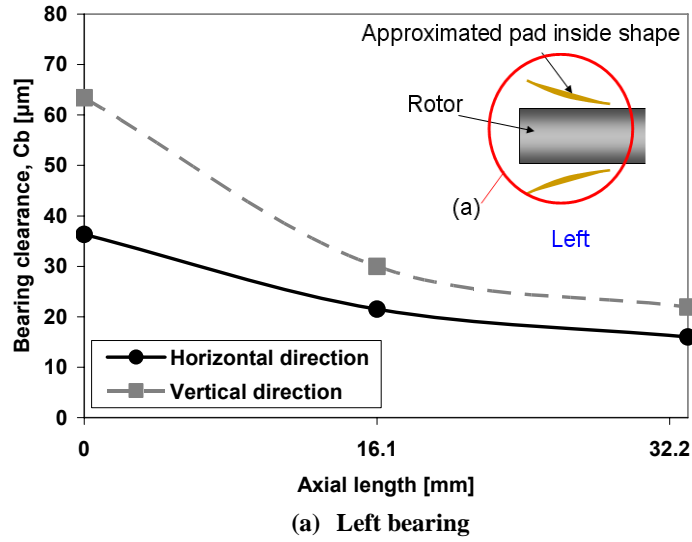


Fig. 4 Estimated radial clearances and axial shape of pads in test bearings

Table 2. List of sensors gains

Name	Location	Sensitivity	Unit
<u>Force</u> Transducers	Left Bearing for vertical direction	119	mV/N
	Right Bearing for vertical direction	120	mV/N
<u>Displacement</u> eddy current sensors	Left Bearing, vertical direction (LV)	8.5	mV/μm
	Left Bearing, horizontal direction (LH)	8.6	mV/μm
	Right Bearing, vertical direction (RV)	8.7	mV/μm
	Right Bearing, horizontal direction (RH)	8.6	mV/μm

The base plate supporting the test rig can be rotated around a hinge and fixed at a desired angular location, see Figure 5. This feature allows for tests to be conducted with the rotor weight acting along a pad [load on pad (LOP)] when the plate is horizontal, or load in between two pads [LBP] when the base plate is at 45°. Figure 6 depicts schematic views of the two load configurations. Note that LOP and LBP conditions are the most common in practice. The present work intends to determine the differences in rotordynamic performance for the rotor when supported on its bearing for the two static load configurations.

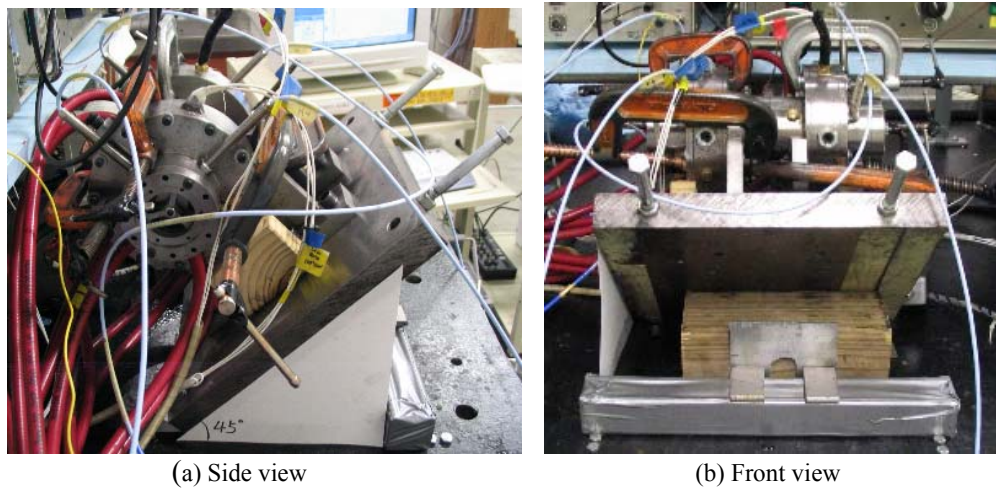


Fig. 5 Rotation of rig for experiments with load-between-pad condition on test bearings

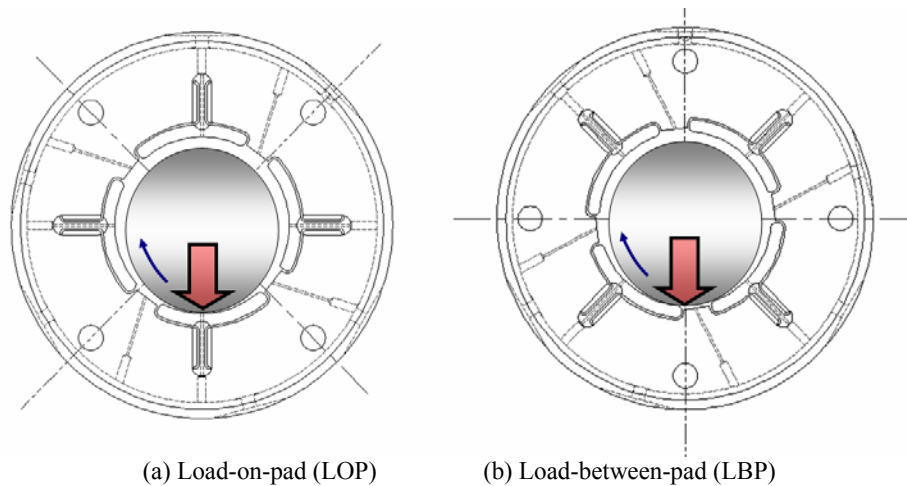


Fig. 6 Bearing configurations for Load-on-pad (LOP) and Load-between-pad (LBP) conditions

Experimental Procedure

Prior to testing, the rotor was balanced in a commercial machine. The balancing was conducted on two planes (rotor ends) at a low speed 1,200 rpm. The residual imbalances at the left and right sides of the rotor are 0.16 g-mm and 0.20 g-mm, respectively. These values satisfy quality grade $G=2.5$ balance tolerance as per ISO 1940/1 ($6.015 G W/(2N)=0.00068$ oz-in=0.491 g-mm) where $W=1.815$ lb is the rotor weight and $N=20,000$ rev/min is the rotational speed. The speed selected is close to the test system second critical speed.

Rotor coast-down speeds tests are conducted for various imbalance conditions and feed supply pressures equal to 2.36, 3.72 and 5.08 bar. It is important to note that within the typical test speed range (< 50 krpm), the test rotor can be regarded as a rigid body. Details on the rotor natural frequencies follow in a later section.

Added masses (m_i) are inserted in the holes located at the rotor ends and at a radial distance (R') of 12 mm. The imbalance displacement (u), i.e. distance from rotor center of mass, is

$$u = \frac{m_i R'}{m_i + M} \quad (1)$$

where M is the rotor mass (0.824 kg). Figure 7 depicts the imbalance mass locations on each rotor end. Table 3 summarizes the imbalance mass and location for the two types of imbalance tests. In test U(A₁)~U(A₃), the imbalance masses are positioned at the same angular location at each rotor end; whereas in test U(B₁)~U(B₃), the imbalance masses on each end are 180° out of phase.

The API permissible residual imbalance ($4W/N$) is just 0.261 g-mm (0.000363 oz-in). Note API requirement is larger than ISO standard. The added masses (m_i) render larger imbalance conditions (0.36 g-mm, 0.41 g-mm, and 0.48 g-mm). At 20 krpm and for the largest added mass (0.04 g), the imbalance force ($2 m_i R' \Omega^2$) equals 4.21 N, i.e. 52 % rotor weight, exceeding the admissible API specification, i.e. “*the maximum admissible unbalance force on any bearing at the maximum continuous speed shall not exceed 10% of the static loading of that bearing.*” Note that satisfying API constraints in small machinery rotating at high speeds is (probably) impractical.

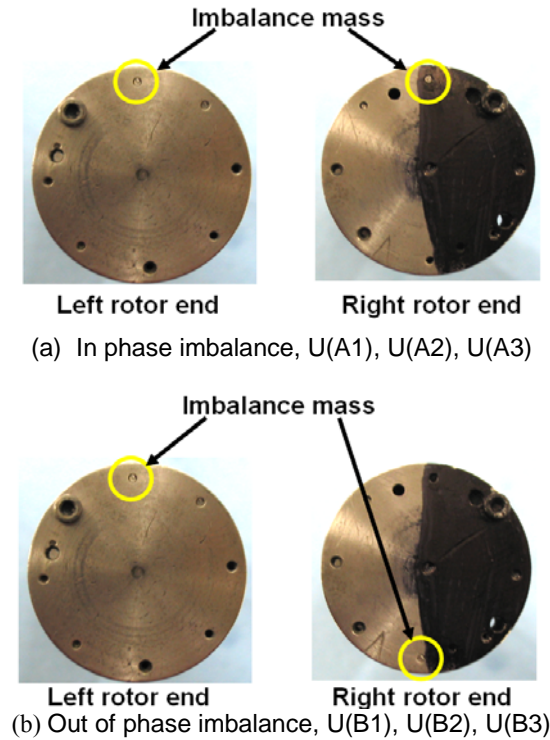


Fig. 7 Locations of imbalance masses at end faces of rotor. (Dark color for triggering infrared tachometer)

Table 3. Imbalance mass magnitudes and locations

Imbalance name	Imbalance mass [g] ($m_{\text{left}}, m_{\text{right}}$) $\pm 0.002\text{g}$	Angular location ($\phi_{\text{left}}, \phi_{\text{right}}$)	Imbalance displacement [μm] (u)
U(A ₁)	0.030, 0.030	0°, 0°	0.43
U(A ₂)	0.034, 0.034	“	0.49
U(A ₃)	0.040, 0.040	“	0.58
U(B ₁)	0.030, 0.030	0°, 180°	0.43
U(B ₂)	0.034, 0.034	“	0.49
U(B ₃)	0.040, 0.040	“	0.58

To prevent damage of the bearings and rotor during speed start-up to a high speed, typically 50 krpm, the supply pressure is maintained at 2.36 bar absolute while the rotor passes through its critical speed(s). This precaution is also in place when the procedure calls for coast down experiments without external pressurization. Once operating well above the critical speed, the feed pressure lines are closed and the rotor runs up to 45,000 rpm. During this operation condition, the bearings work purely in the hydrodynamic film regime.

Experimental Results

Baseline rotor responses

Figure 8 depicts the recorded synchronous amplitudes (0-peak) of rotor motion obtained at a 5.08 bar absolute feed pressure for the LOP condition with slow roll compensation at 4,000 rpm. This response is termed as baseline since it does not include any added imbalance masses. The graph shows the amplitudes recorded on the outer sides of the left and right bearings, and along the horizontal and vertical directions for each bearing. The response for each bearing shows a distinctive single peak at a particular rotor speed. The speeds at which the amplitude peaks along the left vertical (LV), left horizontal (LH), right vertical (RV) and right horizontal (RH) directions are 16,700 rpm, 13,700 rpm, 20,400 and 20,000 rpm, respectively. The multitude of peaks reveals the different dynamic force characteristics from each bearing and also evidences a complicated remnant imbalance distribution. Recall that the clearance on the left bearing (LB) is larger than that of the right bearing (RB), and hence the LB support stiffness must be lower than that of the RB, which explains the lower speed at which the rotor amplitude peaks. Furthermore, also recall that the clearances along the vertical and horizontal directions are different for each bearing.

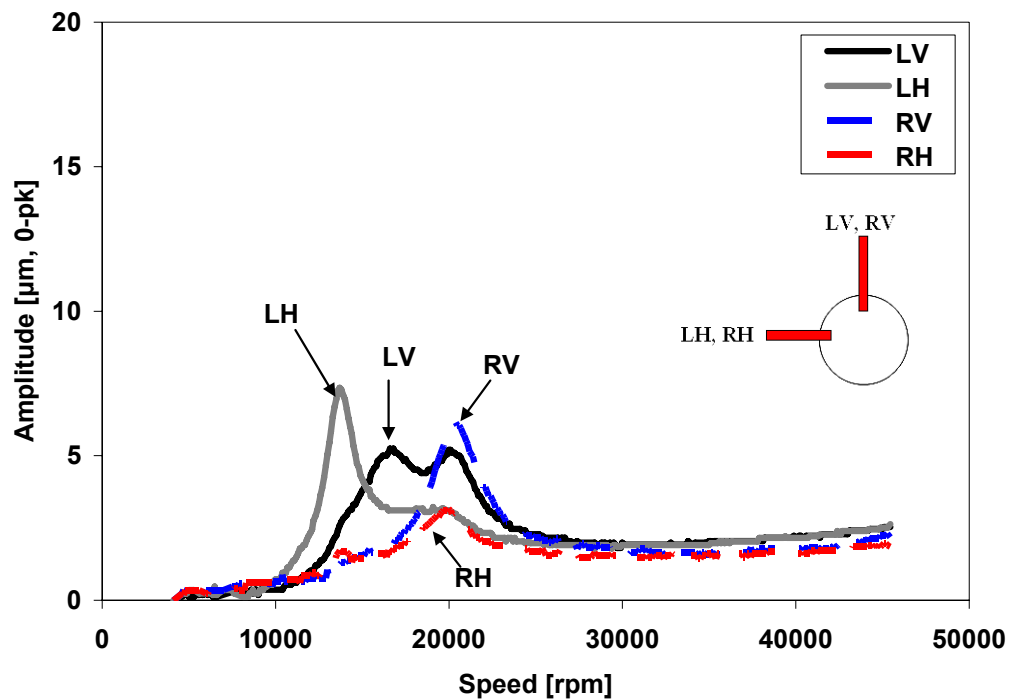


Fig.8 Amplitudes of rotor synchronous response versus speed. Baseline imbalance, LOP condition, 5.08 bar feed pressure, slow roll compensation at 4000 rpm

The rotor is “rigid” within the speed range; and thus, the shape of the synchronous responses can be readily determined by subtracting the phase angles of the measured displacements at the left and right sides of the rotor. Operation with near 0° phase difference indicates a cylindrical mode; while a phase difference of 180° denotes a conical mode. Figure 9 depicts a phase difference of $\sim 180^\circ$ while traversing the speeds with largest amplitudes, and then decreasing steadily towards 45° at the top speed, 45 krpm. Figure 10 displays the ratio of amplitudes between the left and right bearing responses, vertical and horizontal planes. The graphical inserts in Figure 10 intend to portray the shape of the rotor motion at various speeds. Note that only a conical mode occurs while traversing the speed range of peak amplitudes. At the lowest speed, 13.7 krpm, the rotor motions are largest along the horizontal direction on the left bearing. At a speed of 20 krpm, the node in the conical mode moves from the right bearing towards the rotor center; and both amplitudes of motion are nearly identical. At higher speeds, say 45 krpm, the phase difference and amplitude ratio (~ 1) denote operation closely resembling a cylindrical mode.

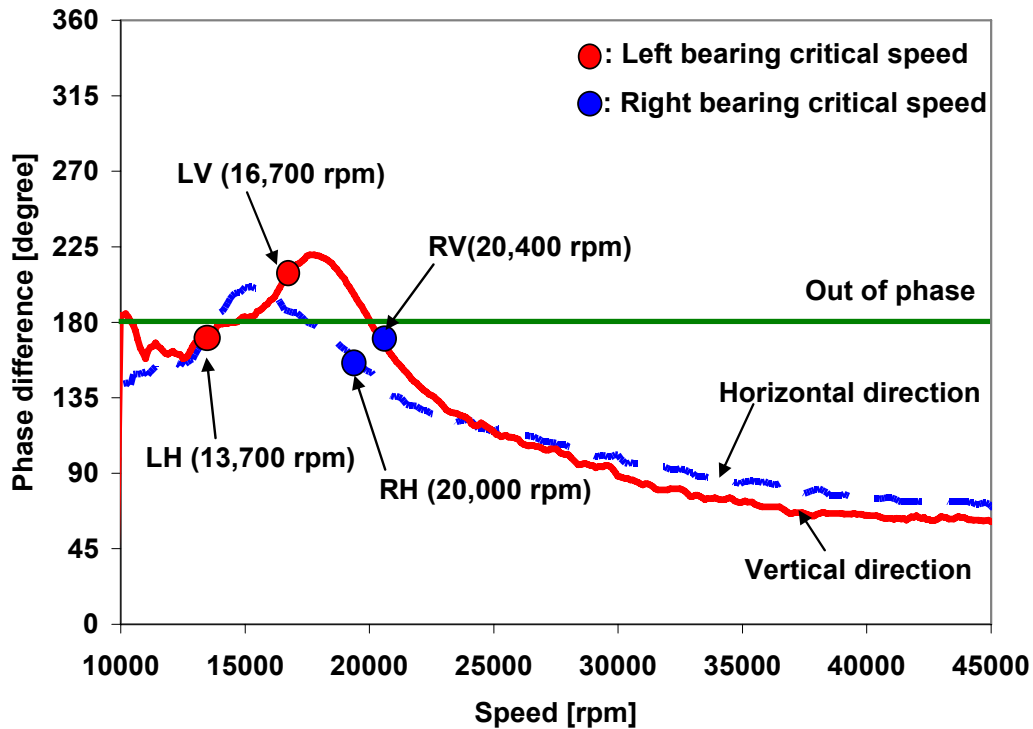


Fig. 9 Phase difference (left – right) of recorded imbalance responses versus speed. Baseline imbalance, LOP condition, 5.08 bar feed pressure, slow roll compensation at 4000 rpm

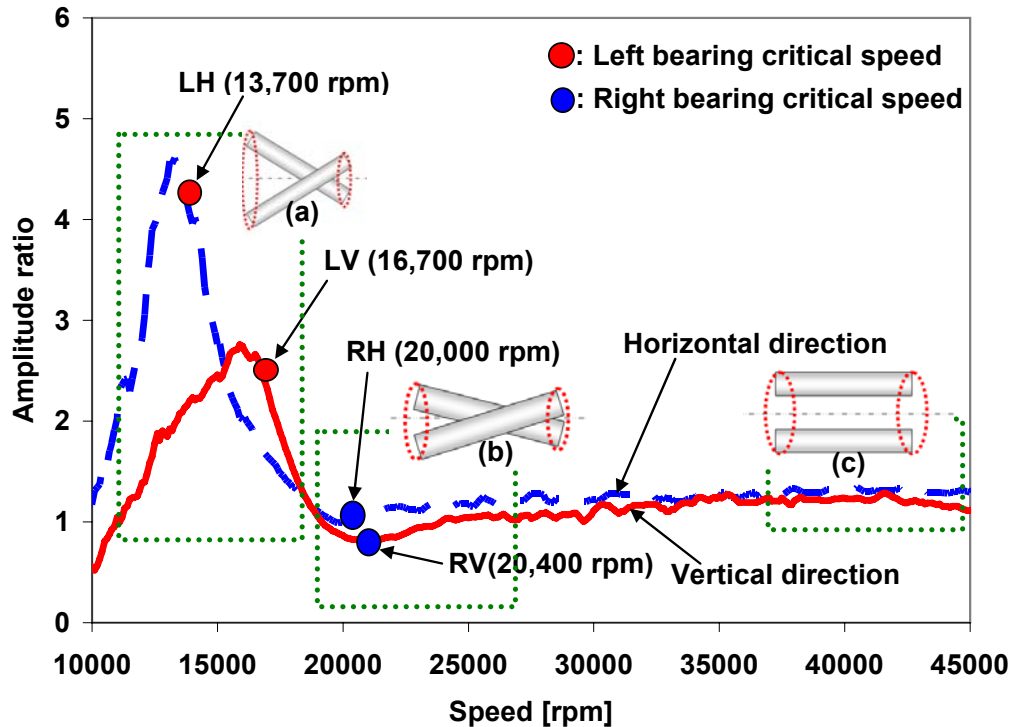


Fig. 10 Amplitude ratio (left / right) of recorded imbalance responses versus speed. Baseline imbalance, LOP condition, 5.08 bar feed pressure, slow roll compensation at 4000 rpm

For the load between pad configuration (LBP), Figure 11 depicts the recorded synchronous amplitudes (0-peak) of rotor motion obtained at a 5.08 bar absolute feed pressure. The graph shows the amplitudes recorded on the outer sides of the left and right bearings, and note that the (LV, RV) and (LH, RH) displacement sensors are located 45°CW and 45°CCW from the vertical plane, respectively. As with the LOP condition, the response for each bearing shows a distinctive single peak at a particular rotor speed. The speeds at which the amplitude peaks along the (LV), (LH), (RV) and (RH) directions are 16,000 rpm, 14,000 rpm, 20,500 rpm and 19,700 rpm, respectively. These speeds are nearly identical to the LOP measured results, and demonstrate that the rotor (light) weight acting on LOP or LBP has little effect on the dynamic forced performance of the test bearings.

Figure 12 displays a waterfall plot depicting the amplitude and frequency content of the rotor motions as its speed drops from 45 krpm towards rest. The measurement corresponds to 5.08 bar pressure and LBP condition. There is a dominance of synchronous motions and small amplitude supersynchronous frequencies. The rotor operation is stable without any subsynchronous vibration, thus demonstrating the test bearings have insignificant cross-coupled stiffness.

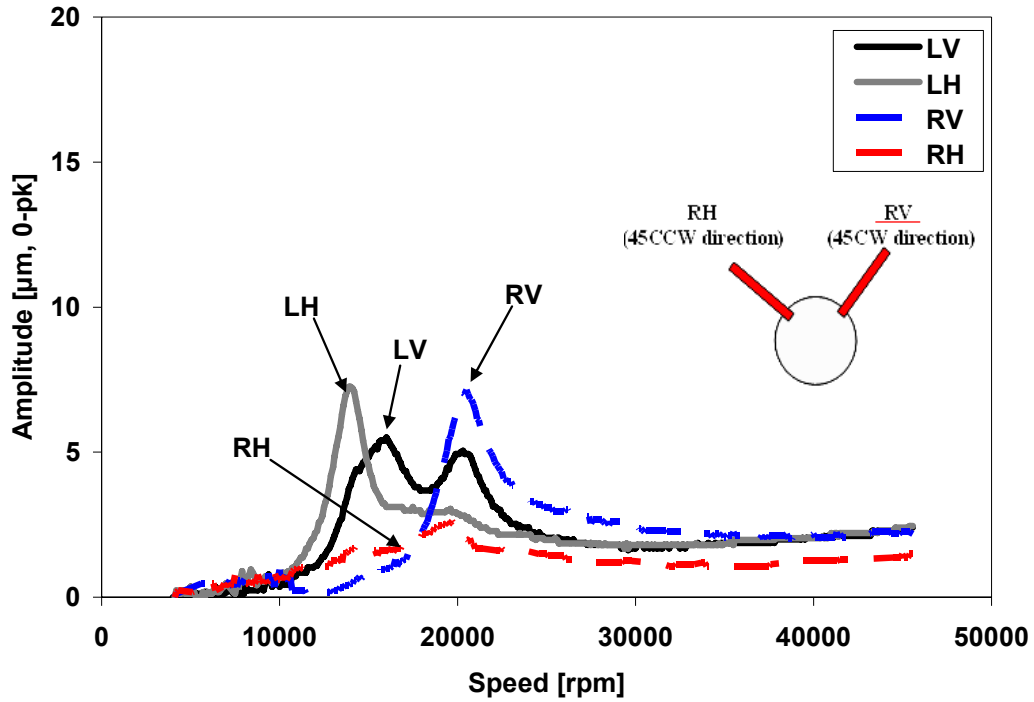


Fig. 11 Amplitudes of rotor synchronous response versus speed. Baseline imbalance, **LBP condition**, 5.08 bar feed pressure, slow roll compensation at 4000 rpm

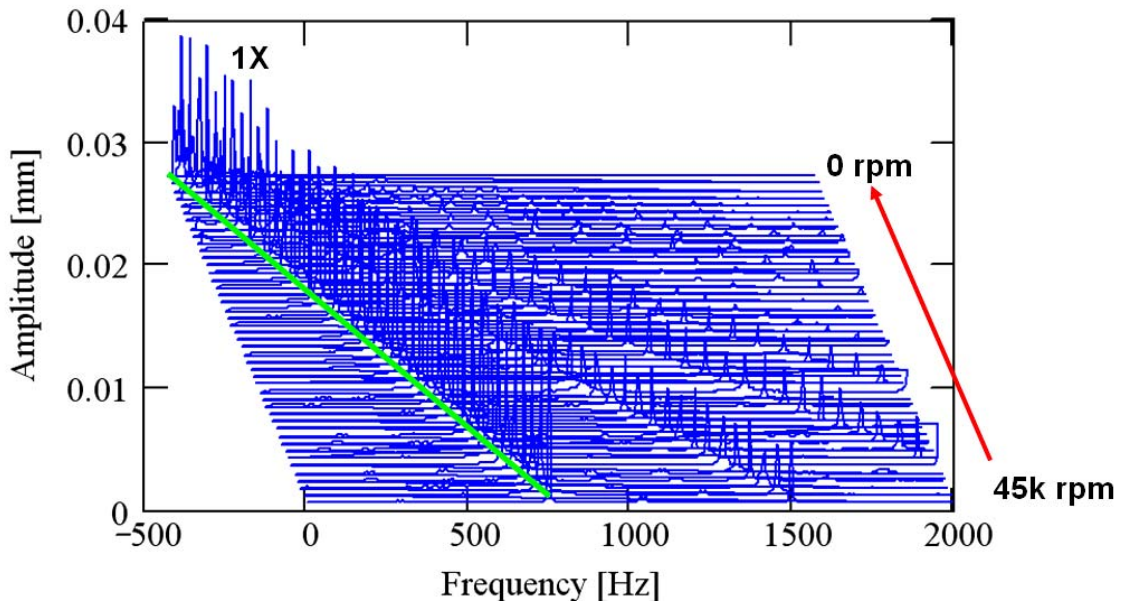


Fig. 12 Waterfall of baseline rotor motions for test with 5.08 bar feed pressure Left bearing, 45°CW plane, LBP condition

Figure 13 and 14 portray the synchronous (1X) rotor orbits for the LOP and LBP conditions while traversing the speeds of peak amplitudes of motion. Note that the orbits for the LOP and LBP configurations are almost identical at nearly similar shaft speeds. The ellipticity of the orbital motions also shows the differences in bearing stiffnesses. AT the top test speed, 45 krpm, Figure 15 depicts the 1X orbits for the LBP and LOP cases. Note the orbits are nearly circular and showing an almost cylindrical mode of vibration (keyphasor marks nearly in phase).

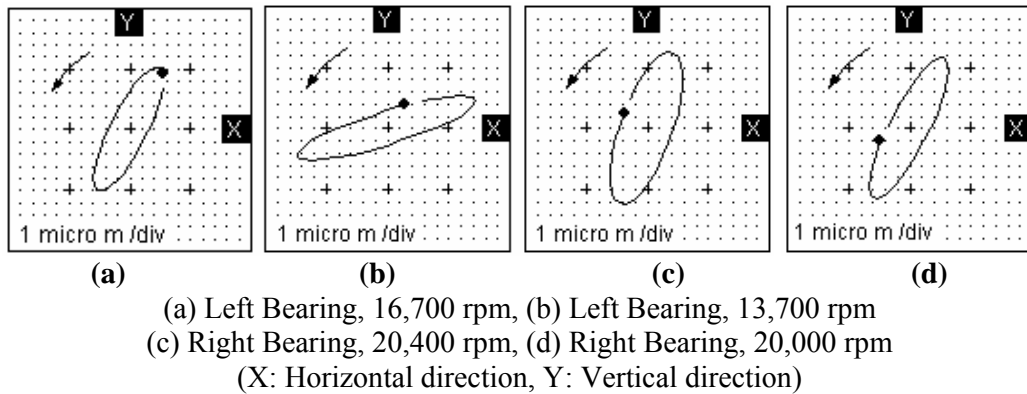


Fig. 13 Synchronous speed rotor orbits for baseline condition, Load on Pad configuration, 5.08 bar feed pressure. Slow roll compensation at 4000 rpm

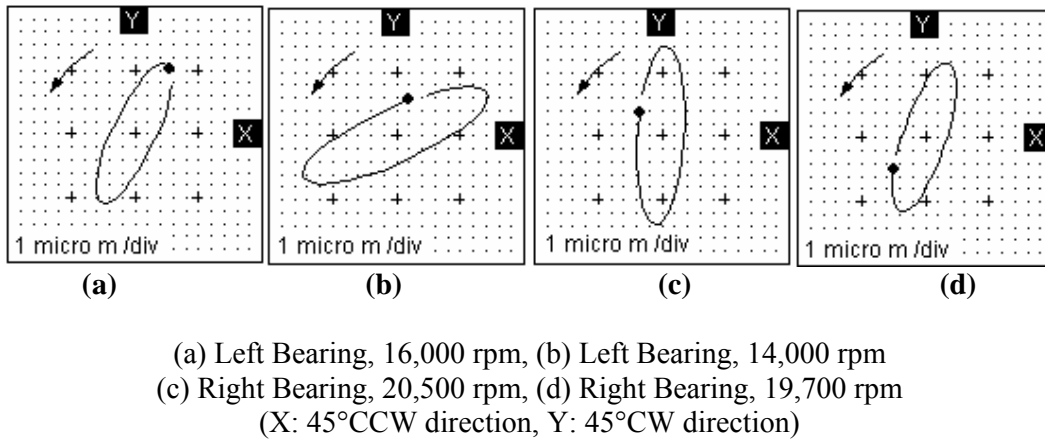
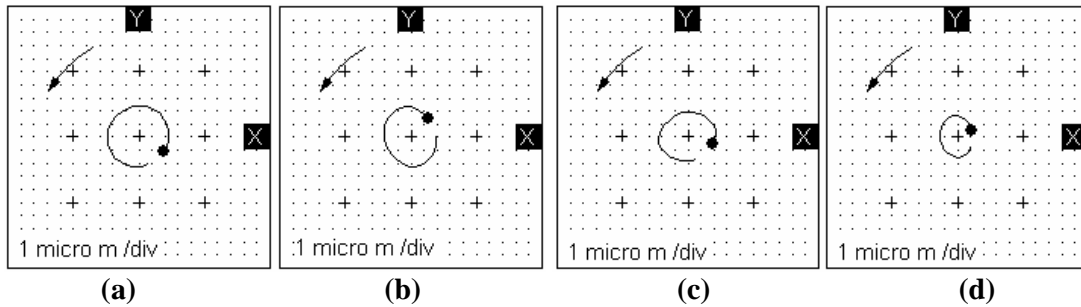


Fig. 14 Synchronous speed rotor orbits for baseline condition, Load on Pad configuration, 5.08 bar feed pressure. Slow roll compensation at 4000 rpm



LOP: (a) Left bearing, (b) Right bearing

LBP: (c) Left bearing, (d) Right bearing

Fig. 15 1X rotor orbits for baseline condition, Load on Pad and Load Between Pads configurations, 5.08 bar feed pressure, 45 krpm shaft speed

Comparison of rotor responses for various supply pressures into the gas bearings

Figures 16 and 17 depict the amplitudes (0-peak) of rotor synchronous motion for increasing feed pressures. The test results correspond to the baseline imbalance condition and the LOP and LBD configurations, respectively. The graphs show responses for three supply pressures into the bearings, 5.08, 3.72 and 2.36 bar (absolute) and no external pressurization.

There is little difference in response amplitude for the two load conditions. As also determined earlier [4], as the supply pressure increases, the gas bearing direct stiffnesses increase, thus the rotor-bearing system critical speed also increases. However, the system damping ratio decreases; and hence, larger peak amplitudes of motion are evident as the supply pressure increases. Note that the critical speed without external pressurization is ~ 10 krpm; while for the largest feed pressure (5 bar), the critical speed is ~ 22 krpm. The 10+ krpm difference offers an opportunity to operate the system with controlled external pressurization to avoid entirely the passage through a critical speed, as shown later.

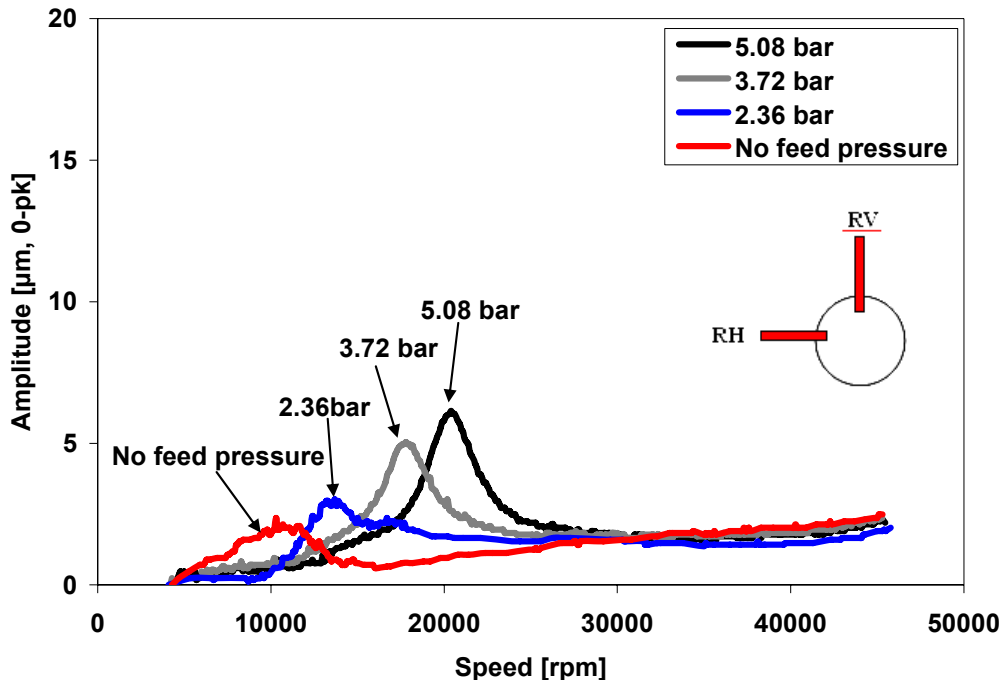


Fig. 16 Effect of increasing supply pressure on test rotor synchronous response. **LOP condition**, Baseline imbalance, slow roll compensation at 4000 rpm. Measurement on side of right bearing (vertical direction)

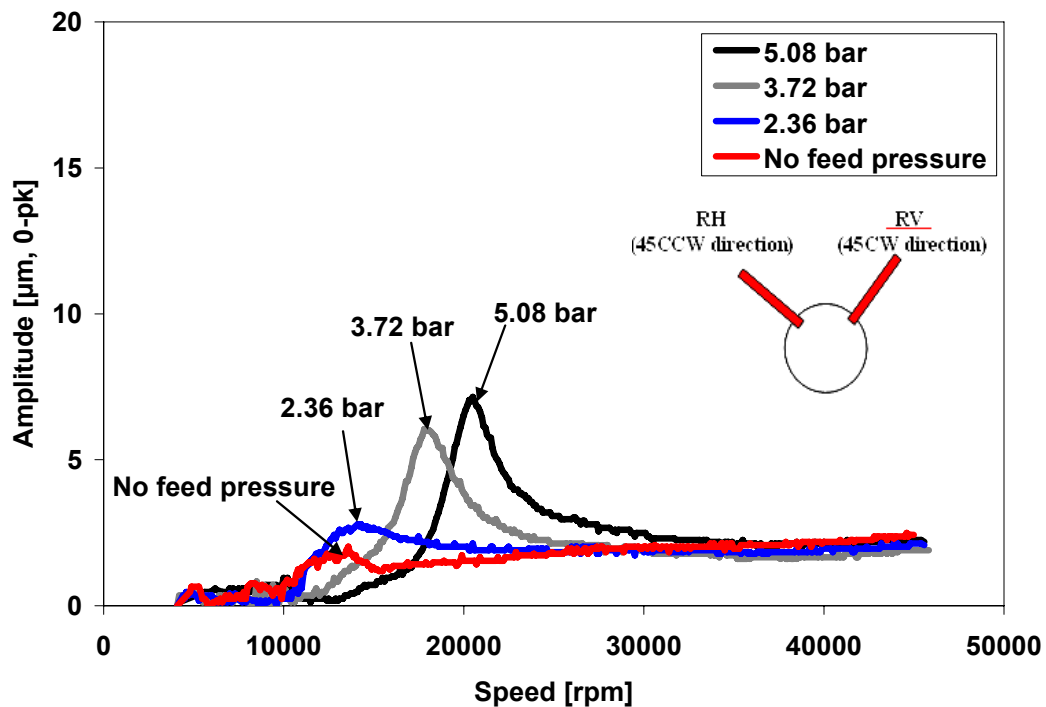


Fig. 17 Effect of increasing supply pressure on test rotor synchronous response. **LBP condition**, Baseline imbalance, slow roll compensation at 4000 rpm. Measurement on side of right bearing (45° CW from vertical)

Rotor responses with added imbalance masses

Table 3 lists the conditions for each test with increasing mass imbalances and in or out of phase location. For imbalance condition U(B₂), see Table 3, Figure 18 depicts the recorded synchronous (0-peak) amplitudes of rotor motion obtained at a 5.08 bar absolute feed pressure for the LOP configuration with slow roll compensation at 4,000 rpm. The graph shows the amplitudes recorded on the outer sides of the left and right bearings, and along the horizontal and vertical directions for each bearing. Note that the imbalance condition equals $u=0.99 \mu\text{m}$ (out of phase). As with the baseline measurements, the response for each bearing shows a distinctive single peak at a particular rotor speed. The speeds at which the amplitude peaks along the left vertical (LV), left horizontal (LH), right vertical (RV) and right horizontal (RH) directions are 16,900 rpm, 13,800 rpm, 21,200 and 22,900 rpm, respectively. The largest amplitude of motion is 16.5 μm (RV), which approaches the minimum estimated bearing radial clearance ($\sim 20 \mu\text{m}$).

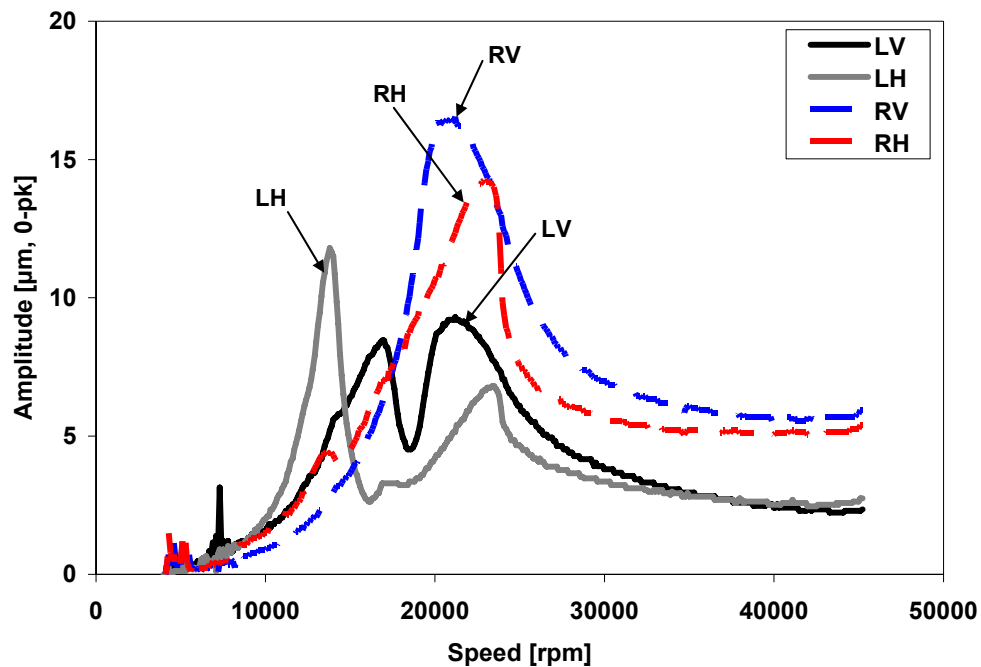


Fig. 18 Amplitudes of rotor synchronous response versus speed. Imbalance U(B₂): 0.034 gram, LOP condition, 5.08 bar feed pressure, slow roll compensation at 4000 rpm

For the LOP condition, Figure 19 and 20 compare the measured peak amplitudes (0-peak) of rotor synchronous response for various imbalances and supply pressure conditions with baseline subtraction. Out-of-phase imbalance condition determines larger rotor motion

amplitudes than for the in-phase imbalance condition. Feed pressure also produces larger amplitudes of rotor response while crossing a critical speed. Note that the peak amplitudes of rotor motion increase linearly with added mass.

Comparisons of other imbalance responses to rotordynamics predictions are given later.

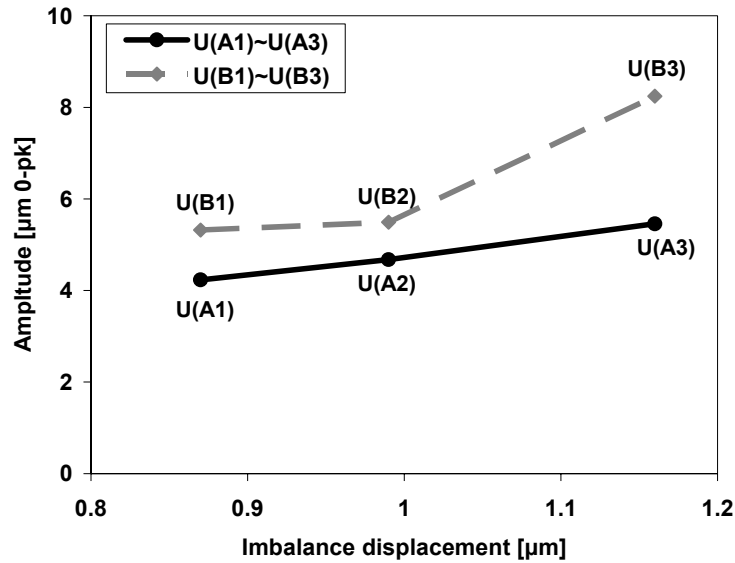


Fig. 19 Effect of increasing imbalance mass on peak amplitude of rotor synchronous response. **LOP condition**. Displacements at left bearing, vertical direction (LV). Baseline response subtracted

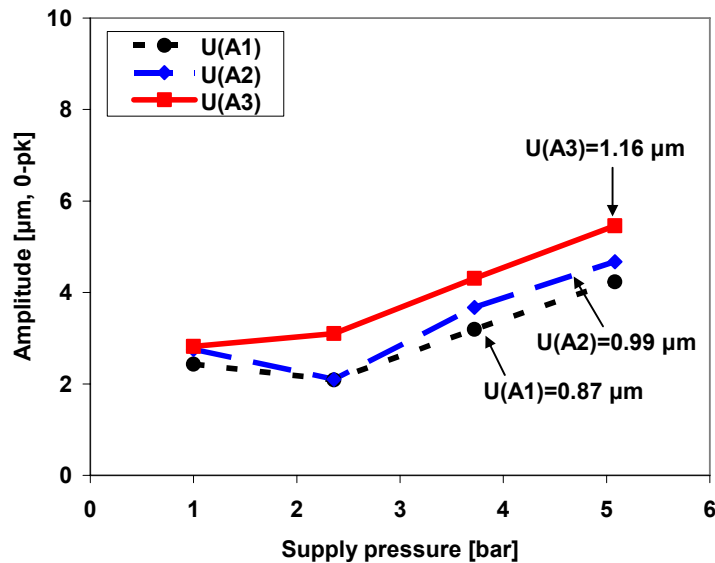


Fig. 20 Comparison of measured peak amplitudes of rotor motion for various imbalances and supply pressure conditions. **LOP configuration**. Displacement at left bearing, vertical direction (LV). Baseline response subtracted

Control of supply pressure to eliminate passage through a critical speed

The imbalance responses acquired for increasing supply pressures suggest the possibility of operating the rotor without actually exciting a critical speed, i.e. without large amplitudes of motion. To this end, experiments are conducted where, as the rotor speed decelerates from its top speed of 45 krpm, the supply pressure is steadily increased from 1.7 bar to 5 bar over a narrow speed range [15 – 10 krpm]. Figure 21 shows the schedule of feed pressure versus rotor speed.

Figure 22 depicts the synchronous amplitude (0-peak) of rotor motion versus shaft speed and with controlled supply pressure into the bearings. The broken lines show the responses also depicted in Figure 16 for supply pressures kept constant over the entire speed range. The present measurements demonstrate the elimination of the speed region where the amplitudes peak, i.e. no excitation of a critical speed. Note the remarkable reduction on amplitude of motion in the speed range from 20 krpm to 12 krpm.

The measurements evidence the benefits of a controlled operation of the rotor bearing system. In practice, external pressurization is only needed at low rotor speeds to ensure rotor lift off as well as to increase the system critical speed. At high speeds, external pressurization can be brought to a minimum, without affecting the dynamic response of the system.

Note that the rotor response measurements were conducted under quasi static conditions. The results presented do not actually represent a true coast down speed response, The change from high to low feed pressure versus rotor speed must be automated with due attendance to the time needed to eliminate a critical speed while the rotor accelerates or decelerates.

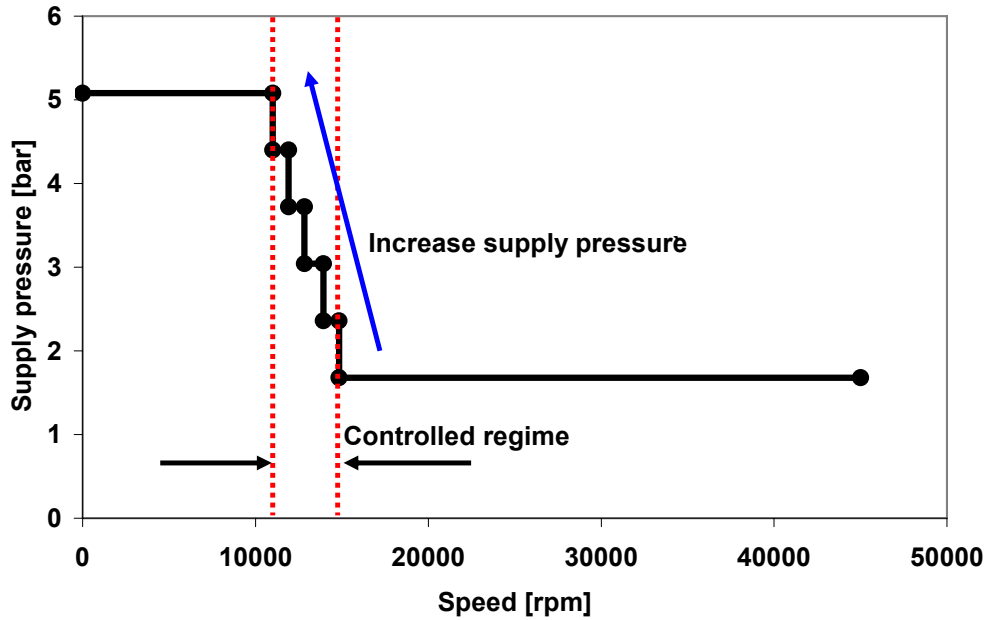


Fig. 21 Manual changes in supply pressure as rotor speed coasts down

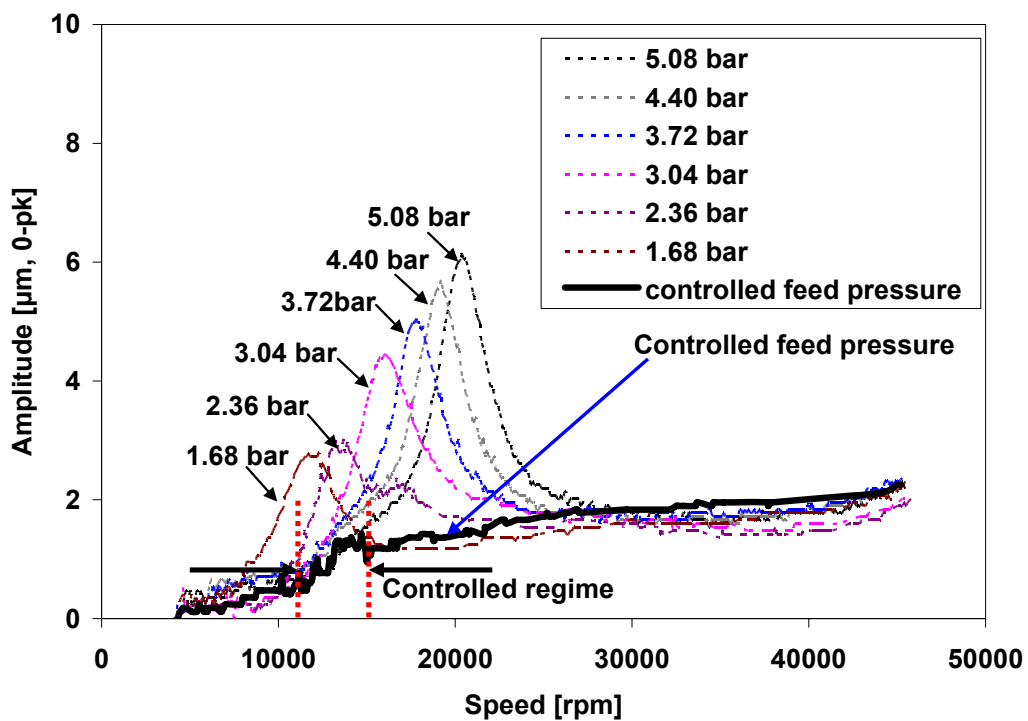
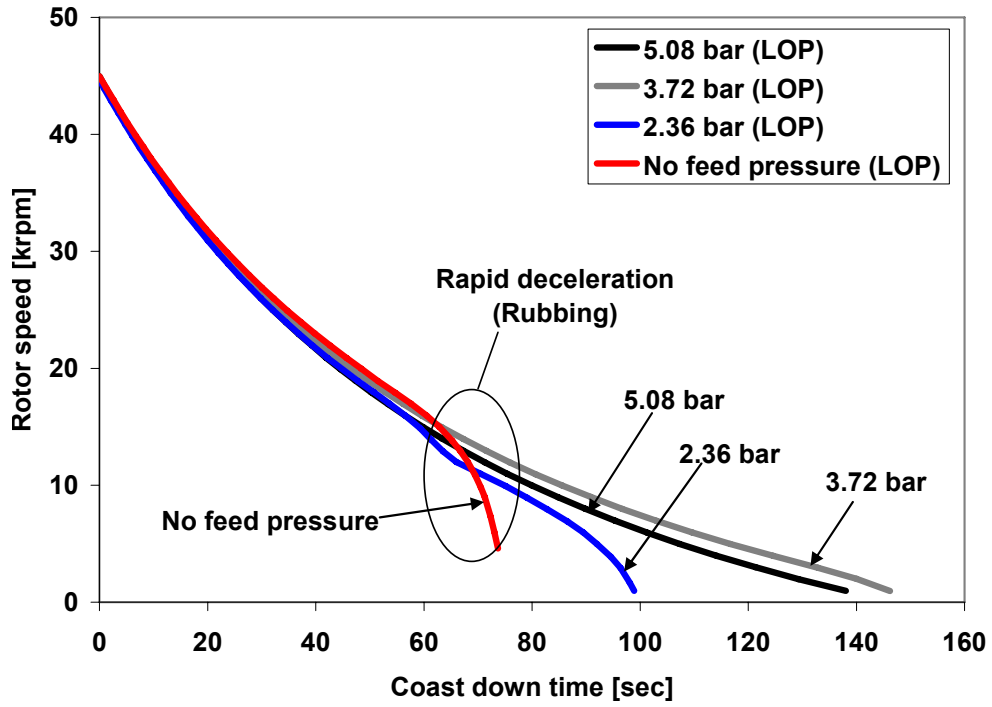


Fig. 22 Amplitudes of rotor synchronous response versus speed for controlled feed pressures. **LOP condition**, Baseline imbalance, slow roll compensation at 4,000 rpm. Measurements at right bearing side, vertical direction (RV)

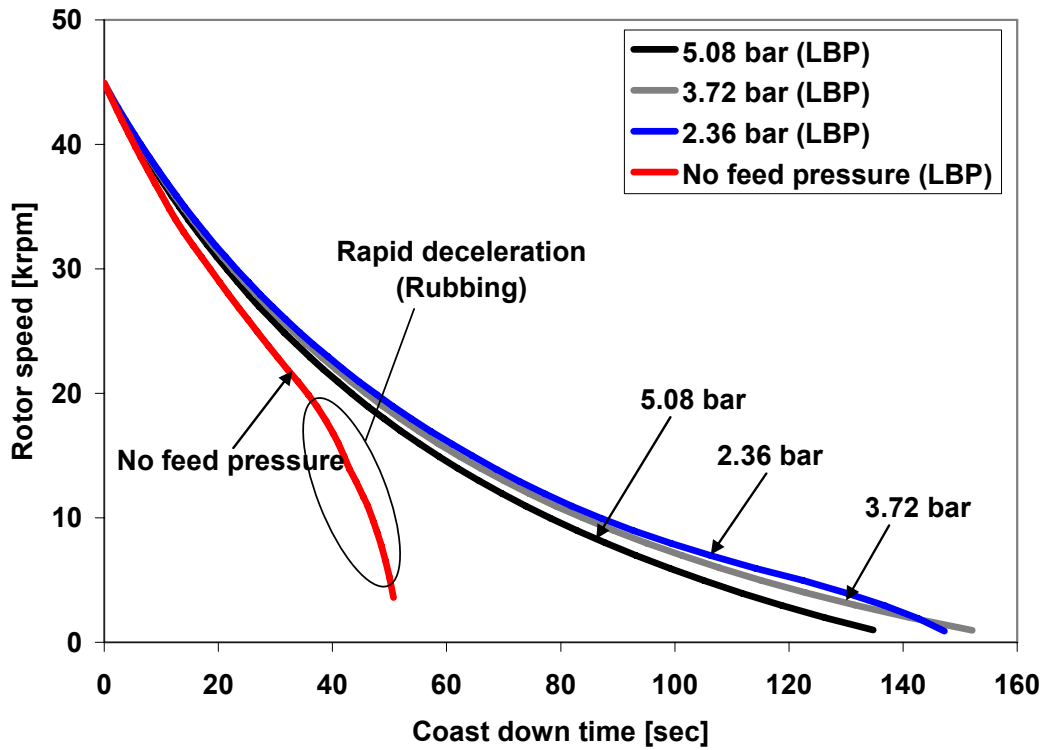
Coast down rotor speed and type of drag

Figures 23 depict the rotor coast down speed curves versus time for increasing gas feed pressures and for the LOP and LBP configurations. The time for the rotor to coast down is quite large, over 2 minutes, as long as the gas bearings are pressurized. That is, external pressurization ensures a low drag friction operation over the entire speed range. For the highest supply pressures, 3.72 bar and 5.08 bar, there are little differences in the recorded speeds for the LOP and LBP configurations. The rotor coast down curves show a decaying exponential shape, typical of a rotational system with viscous drag. Note that for feed pressure of 2.36 bar, the rotor-bearing with LOP bearings decelerates faster than for the LBP configuration. Most notably however, is the rapid rotor deceleration when the gas bearings are not pressurized, in particular for the LBP configuration. For speeds below 15 krpm, the rotor versus time relationship is linear, typical of dry-friction (rubbing condition).

Figure 24 compares the rotor speed coast-down curves for three mass imbalance conditions. The coast down time is identical for the baseline imbalance and calibrated in-phase imbalance $U(A_3)$. However, for the out of phase imbalance, $U(B_3)$, there is a temporary rubbing condition while traversing the critical speed, with a quick deceleration from 20 krpm to 17 krpm. The transient rubbing condition is due to the large amplitudes of motion while traversing the system critical speed. Note that for speeds below 15 krpm, the rotor speed shows the typical exponential decay, indicative of no contact (viscous-like operation).



(a) Load-on-pad configuration



(b) Load-between-pad configuration

Fig. 23 Effect of supply pressure on length of coast-down rotor deceleration. (a) LOP and (b) LBP configurations. Baseline imbalance

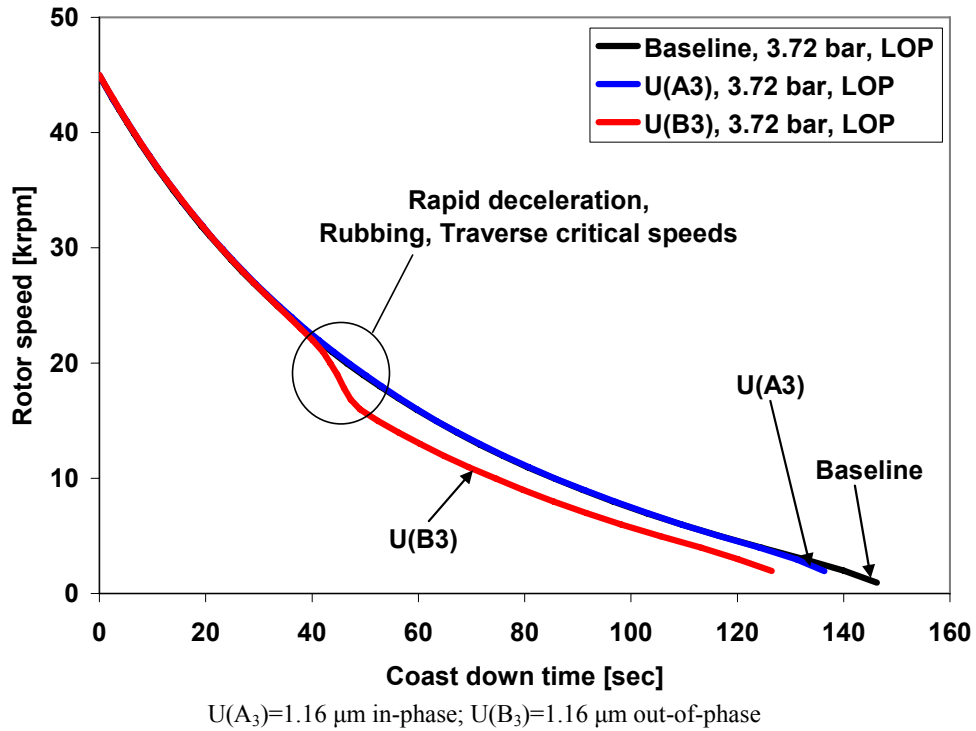


Fig. 24 Comparison of rotor speed coast-down curves versus time for various imbalance conditions (baseline, U(A₃) and U(B₃)) at 3.72 bar absolute feed pressure (LOP configuration)

Predictions of rotordynamic response and comparison to test results

TILTPADHGB© is a FORTRAN program to predict the static and dynamic forced response of fixed or tilting pad gas bearings (hydrostatic, hydrodynamic or both). An EXCEL® graphical user interface handles the user input and FORTRAN output calculations. San Andrés [25] details the analysis and numerical method for this computational program.

Table 1 presents the bearing dimensions and Table 4 below details the assumed radial clearances and preload for the test bearings. The magnitudes noted are representative only since the clearances for both bearings vary along the axial and circumferential directions, as shown in Figure 4.

Table 4 Assumed clearance and preload for prediction of force coefficients for test bearings

Bearing	Radial Clearance, $C_p = R_p - R_j$	Pad preload (0.30)
Right	38.0 μm	11.4 μm
Left	44.5 μm	13.3 μm

Mass flow rate

Figure 25 depicts the predicted and measured mass flow rate for increasing feed pressures. The mass flow rate to the left bearing is larger than that of the right bearing because of the differences in clearances and assembly condition. The predictions agree well with the measurements, thus lending credence to the inherent orifice flow model in the analysis.

Note that a reduced flow rate denotes also a reduction in the gas film pressure acting on the bearing at the orifice location. This reduction in pressure will cause (in general) a drop in bearing direct stiffnesses.

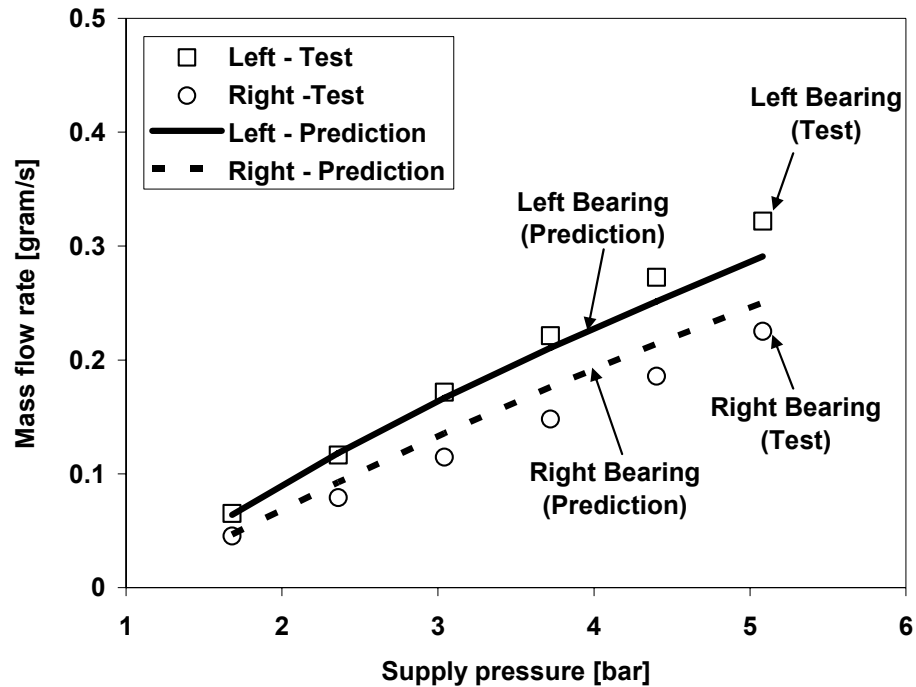


Fig. 25 Measured and predicted mass flow rates versus supply pressure for test bearings (LOP configuration)

Rotor model: Free-free mode natural frequencies and shapes

The test rotor-bearing system is modeled in XLTRC² rotordynamic software. Figure 26 shows the 24 finite element structural model of the composite test rotor. Impact tests with the rotor hanging from long wires are performed to determine its first and second free-free natural frequencies and corresponding mode shapes.

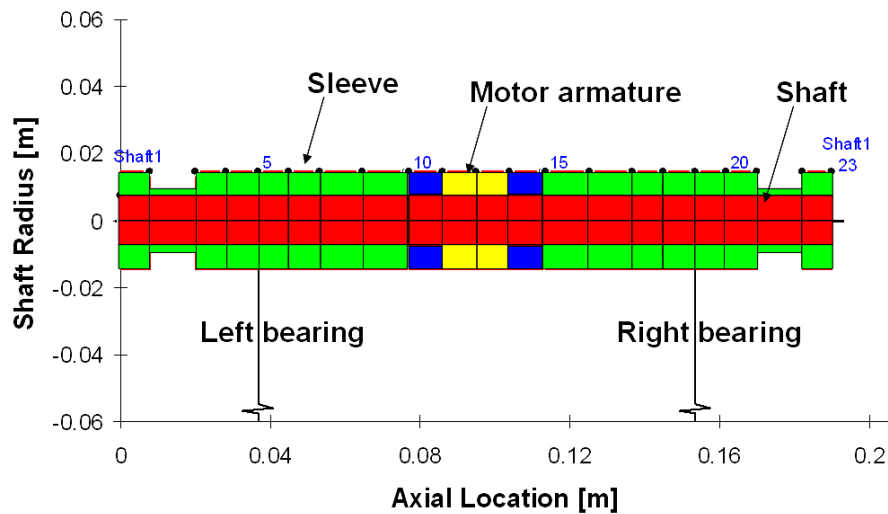


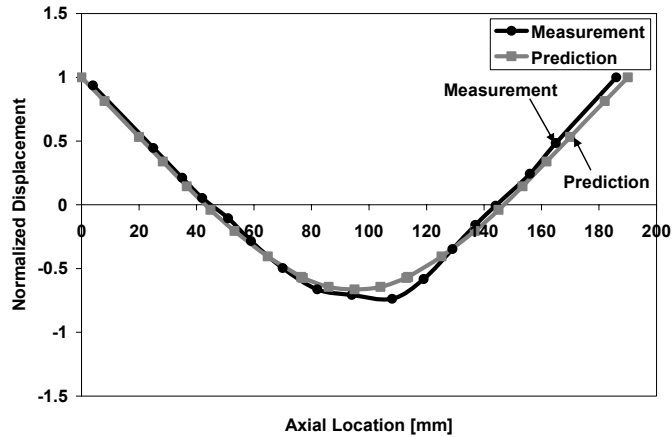
Fig. 26 Structural model of test rotor

Table 5 lists the free-free model natural frequencies obtained from rap tests and predictions from XLTRC². The measured results evidenced good correlation with prediction. Figures 27 display the free-free mode shapes from the rap tests and predictions. Predictions compare very well with measurements. The test data thus validates the rotor structural model. Furthermore, the measurements show the rotor can be regarded as rigid over the speed range of tests (< 50 krpm).

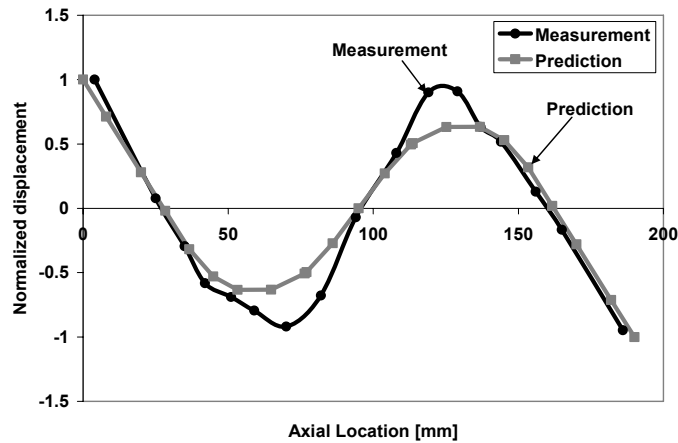
Table 5 Comparison of measured and predicted free-free mode natural frequencies

	Measured	Predicted	Difference
First frequency	1.920 kHz	1.953 kHz	1.73%
Second frequency	6.117 kHz	6.134 kHz	0.28%

Uncertainty in measurements ± 16 Hz



(a) First Free-Free mode (P: 1.95 kHz, T: 1.92 kHz)



(a) Second Free-Free mode (P: 6.13 kHz, T: 6.11 kHz)

Fig. 27 Measured and predicted free-free mode shapes for test rotor

Appendix A includes the (synchronous speed) rotordynamic force coefficients predicted for the gas bearings (left and right) and for three supply pressures, LOP and LBP configurations.

Damped natural frequencies and damping ratios

Figure 28 and Figure 29 show the predicted damped natural frequency and damping ratios of the test rotor-bearing system. The critical speeds are 16.2 krpm and 20.1 krpm, and correspond with conical rigid body modes, as depicted in Figure 30. The conical modes reproduce closely the recorded shapes, as noted in the graph insets of Figure 10. The appearance of the two conical modes is a direct consequence of the difference in force coefficients in the left and right bearings.

Note that critical speeds and damping ratios are identical for the LOP and LBP configurations, since the bearing force coefficients for the LOP condition are nearly identical to those for the LBP condition. The static load acting on each bearing is rather small, and hence the rotor operates at a nearly centered condition.

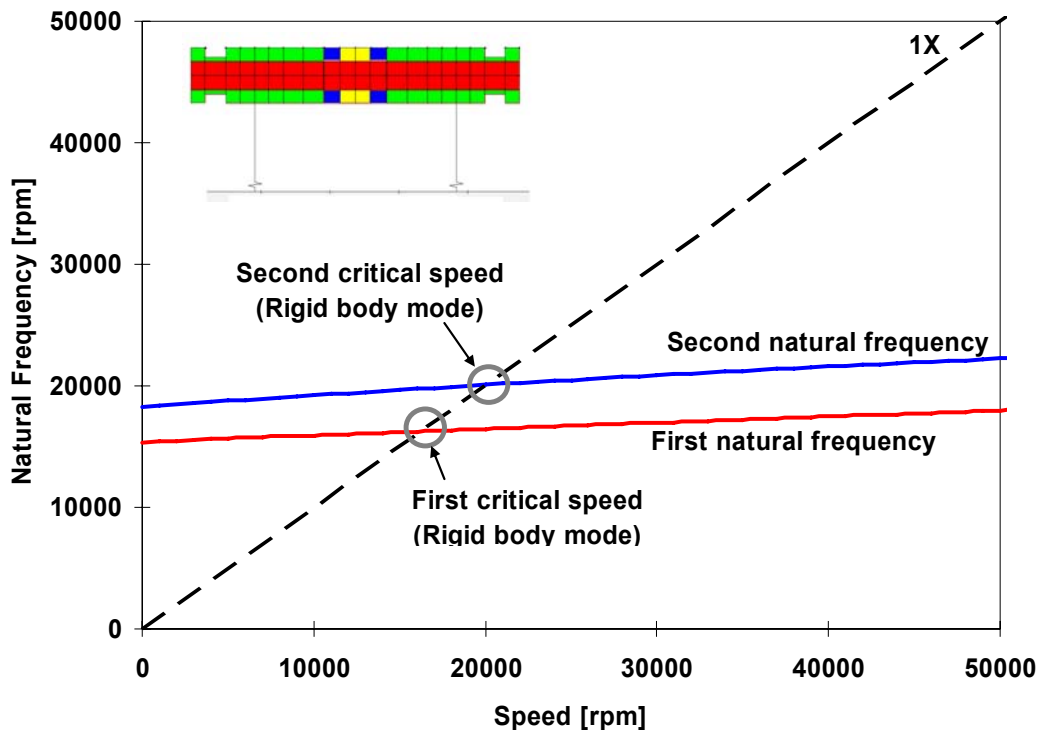


Fig. 28 Damped natural frequency map of test rotor-bearing system. 5.08 bar feed pressure. LOP configuration

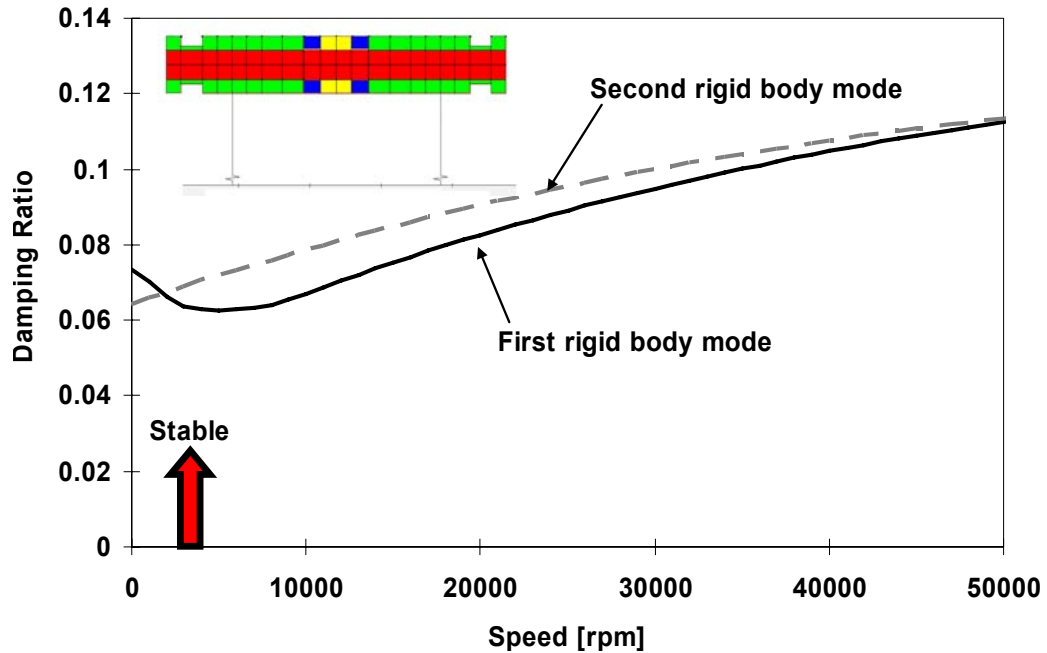


Fig. 29 Predicted damping ratios versus rotor speed. 5.08 bar feed pressure. **LOP configuration**

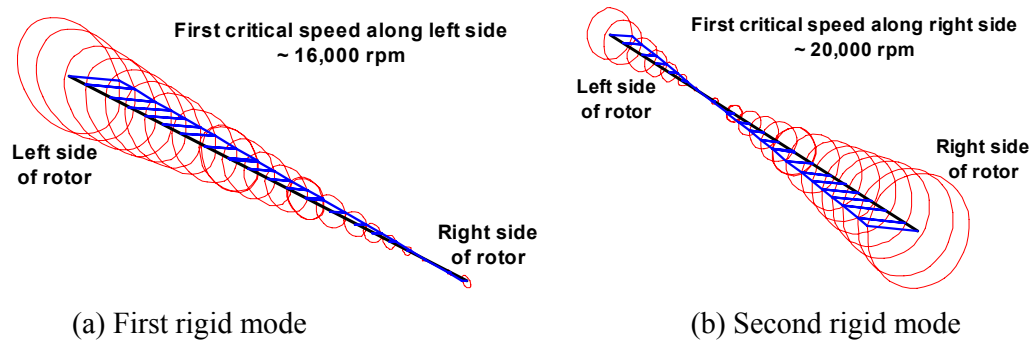


Fig. 30 Mode shapes of rotor at critical speeds. 5.08 bar feed gas pressure. **LOP configuration**

Comparison between predictions and measured imbalance responses

Figure 31 depicts the measured and predicted amplitudes (0-pk) of synchronous response at the left bearing (vertical direction) for the out-of phase imbalance conditions, $U(B_{1,2,3})$. The baseline condition is subtracted from the measured imbalance response to estimate the response due to the imbalance mass added. Note that this consideration is only valid in linear systems. The predictions show a remarkable agreement in the location of the critical speeds and the peak amplitudes of motion.

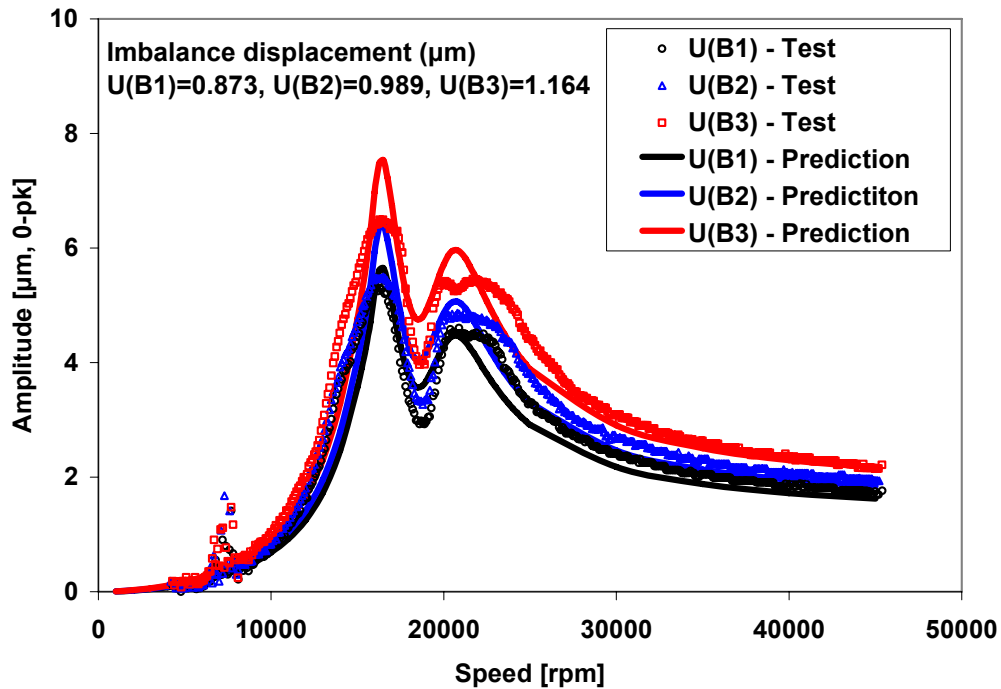


Fig. 31 Predicted and measured imbalance response for three mass imbalance conditions, $U(B_1)=0.43 \mu\text{m}$, $U(B_2)=0.49 \mu\text{m}$, $U(B_3)=0.58 \mu\text{m}$. Tests at 5.08 bar feed pressure (LOP configuration). Displacements at left bearing, vertical direction (LV). Baseline response subtracted

The linearity of the test rotor-bearing system response is verified by normalizing the amplitudes of motion, as shown in Figure 32. The graph depicts the responses obtained for imbalance masses $U(B_{x=2,3})$ multiplied by the ratio of added masses, $U(B_{x=2,3})/U(B_1)$. The three measured results show nearly identical curves, thus denoting the rotor response amplitude of motion is proportional to the mass imbalance. Note that the rotor-gas bearing linearity in response is most unusual considering the large amplitudes of motion recorded (40% of bearing clearance), in particular for the largest imbalance $U(B_3)$.

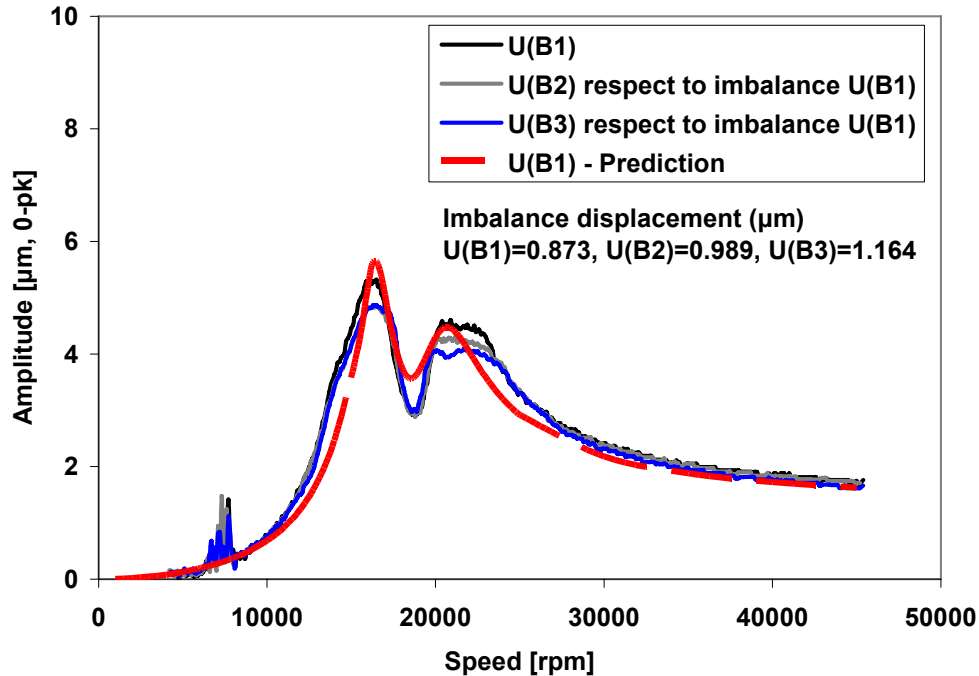


Fig. 32 Predicted and measured normalized imbalance responses, $U(B_3)= 0.58 \mu\text{m}$ and $U(B_1)=0.48 \mu\text{m}$. Tests at 5.08 bar feed pressure (LOP configuration). Displacements at left bearing, vertical direction (LV). Baseline response subtracted

Conclusions

Experiments on a test rotor, 0.825 kg and 28.6 mm diameter, supported on hybrid flexure pivot tilting pad gas bearings are performed for various mass imbalances, increasing feed gas pressures, and under load-on-pad (LOP) and load-between-pad (LBP) configurations. From prior testing, the gas bearings show sustained wear with have uneven pad shapes and dissimilar clearances along the axial and circumferential directions. The changes in clearances affect the static and dynamic performance characteristics of the rotor-bearing system. In the coast down rotor responses with initial speed at 50 krpm, the rotor traverses critical speeds corresponding to rigid body modes, conical and cylindrical-conical. There are no noticeable differences in rotor response for the LOP and LBP configurations due to the light-weight rotor; i.e. low static load acting on each bearing. External pressurization into the bearings increases their direct stiffnesses and reduces their damping, while raising the system critical speed and lessening the viscous damping ratio. Extended times, over two minutes, for rotor coast downs with the bearings pressurized demonstrate the little drag typical of gas bearings. Manual rotor deceleration tests with changes in external

pressurization are conducted to eliminate passage through a critical speed where the rotor motion peaks. This important demonstration paves a way to operate oil-free turbomachinery with controlled external pressurization at high speeds and avoiding the excitation of system critical speeds.

A computational program for modeling of hydrostatic/hydrodynamic flexure pivot tilting pad gas bearings predicts the rotordynamic coefficients of the test bearings. A finite element structural model for the test rotor shows free-free mode elastic modes and natural frequencies matching well measurements. The model links synchronous bearing force coefficients to predict the imbalance response of the test rotor-bearing system. Predicted mass flow rates are in good agreement with measurements.

With external pressurization (pressure supply > 2 bar), predicted bearing force coefficients are nearly identical for both LOP and LBP configurations within the test speed range (< 50 krpm) since the static load acting on each bearing is rather low. Force coefficients for the condition without external pressure (hydrodynamic case) differ considerably from those with external pressurization and between the LOP and LBP configurations. Predicted critical speeds and peak amplitudes of synchronous rotor motion agree well with the measurements. The synchronous rotor response for increasing imbalance masses verifies the test rotor-bearing system's linearity for in-phase and out-of-phase imbalance conditions.

Flexure pivot tilting pad gas bearings are mechanically complex and costlier than rigid surface multiple pad bearings, but their superior stability and predictable static and dynamic characteristics can stimulate successful development of high performance micro-turbomachinery.

References

- [1] Tanaka, S., Isomura, K., Togo, S., and Esashi, M., 2004, "Turbo Test Rig with Hydroinertia Air Bearings for a Palmtop Gas Turbine," *Journal of Micromechanics and Microengineering*, **14**, pp. 1449-1454.
- [2] Wilde, D. A., and San Andrés, L., 2003, "Experimental Response of Simple Gas Hybrid Bearings for Oil-Free Turbomachinery," ASME Paper GT 2003-38833.
- [3] Wilde, D. A., San Andrés, L., and Aguirrezabala, J., 2004, "Experimental Lift Off Characteristics and the Effect of a Low Friction Coating on the Startup Response of Simple Gas Hybrid Bearings for Oil-Free Turbomachinery," ASME paper GT2004-54183.
- [4] Zhu, X., and San Andrés, L., 2004, "Rotordynamic Performance of Flexure Pivot Hydrostatic Gas Bearings for Oil-Free Turbomachinery," ASME paper GT 2004-53621.
- [5] Zhu, X., and San Andrés, L., 2005, "Experimental Response of a Rotor Supported on Rayleigh Step Gas Bearings," ASME Paper GT2005-68296.
- [6] Hamrock, B. J., 1994, *Fundamentals of Fluid Film Lubrication*, McGraw-Hill, New York.
- [7] Zhang, Q., Guo, G., and Bi, C., 2005, "Air Bearing Spindle Motor for Hard Disk Drives," *STLE Tribology Transactions*, **48**, pp. 468-473.
- [8] Powell, J. W., 1970, "A Review of Progress in Gas Lubrication," *Review of Physics in Technology*, **1**, pp. 96-129.
- [9] Gross, W. A., 1969, "A Review of Developments in Externally Pressurized Gas Bearing Technology since 1959," *ASME Journal of Lubrication Technology*, **91**, pp. 161-165.
- [10] Fuller, D. D., 1969, "A Review of the State-of-the-Art for Design of Self-Acting Gas-Lubricated Bearing," *ASME Journal of Lubrication Technology*, **91**, pp. 1-16.
- [11] Gunter, E. J., Castelli, V., and Fuller, D. D., 1963, "Theoretical and Experimental Investigation of Gas-Lubricated, Pivoted-Pad Journal Bearings," *ASLE Transactions*, **6**, pp. 346-357.
- [12] Gunter, E. J., Hinkle, J. G., and Fuller, D. D., 1964, "The Effect of Speed, Load, and Film Thickness on the Performance of Gas-Lubricated, Tilting-Pad Journal Bearings," *ASLE Transactions*, **7**, pp. 353-365.
- [13] Lund, J. W., 1964, "Spring and Damping Coefficient for the Tilting-Pad Journal Bearing," *ASLE Transactions*, **7**, pp. 342-352.
- [14] Pitts, G., 1970, "A Design Method for Tilting-Pad Gas Journal Bearings," *Tribology*, pp. 8-21.
- [15] Lund, J. W., 1968, "Calculation of Stiffness and Damping Properties of Gas Bearings," *ASME Journal of Lubrication Technology*, **90**, pp. 793-80.

- [16] Shapiro, W., 1969, "Steady-State and Dynamic Analyses of Gas-Lubricated Hybrid Journal Bearings," *ASME Journal of Lubrication Technology*, **91**, pp.171-180.
- [17] Zeidan, F. Y., 1992, "Developments in Fluid-Film Bearing Technology," *Turbomachinery International*, **9**, pp. 24-31.
- [18] Armentrout, R. W., and Paquette, D. J., 1993, "Rotordynamic Characteristics of Flexure-Pivot Tilting-Pad Journal Bearings," *STLE Tribology Transactions*, **36**, pp. 443-451.
- [19] Chen, W. J., 1995, "Bearing Dynamic Coefficients of Flexible-Pad Journal Bearings," *STLE Tribology Transactions*, **38**, pp. 253-260.
- [20] Choudhury, P. D., Raouf, H. M., and Paquette, D. J., 1992, "A Flexible Pad Bearing Systems for a High Speed Centrifugal Compressor," *Proceedings of the Twenty-First Turbomachinery Symposium*, pp. 57-64.
- [21] Chen, W. J., Zeidan, F. Y., and Jain, D., 1994, "Design, Analysis, and Testing of High Performance Bearings in a High Speed Integrally Geared Compressor," *Proceeding of the Twenty-Third Turbomachinery Symposium*, pp. 24-31.
- [22] Kepple, K. E., Agahi, R., Ershagih, B., and Zeidan, F. Y., 1998, "Experience in the Use of Flexure Pivot Tilt Pad Bearings in Boiler Feedwater Pumps," *Proceeding of the Fifteenth International Pump Users Symposium*, pp. 77-83.
- [23] Kim, T. H., and San Andrés, L., 2005, "Heavily Loaded Gas Foil Bearings: a Model Anchored to Test Data," *ASME Paper GT 2005-68486*.
- [24] San Andrés, L., Rubio, D., and Kim, T. H., 2006, "Rotordynamic Performance of a Rotor Supported on Bump Type Foil Gas Bearings: Experiments and Predictions," *ASME Paper GT 2006-91238*.
- [25] San Andrés, L., 2005, "Hybrid Tilting Pad Gas Bearings: Analysis and Experimental Validation," TRC-B&C-1-05, Turbomachinery Laboratory, Texas A&M Univ., College Station, TX.

Appendix A

Predicted bearing stiffness and damping force coefficients

Figures A.1 and A.2 depict the predicted the LOP and LBP journal eccentricities and attitude angles versus rotor speed for increasing gas feed pressures. The applied static load on each bearing is 4.042 N, i.e. half the rotor weight. Note that the maximum dimensionless eccentricity is 0.70 for the pure hydrodynamic condition and lowest speed, 10 krpm. Recall that the clearances for both bearings are different (LB: 44.5 μm , RB: 38 μm), and hence the actual physical values of rotor eccentricity differ. Hydrostatic pressurization leads to smaller journal eccentricities, nearly independent of rotor speed; and importantly enough, without significant differentiation for the LOP and LBP configurations. .

The attitude angle is largest for the no feed pressure condition, though nearly invariant with shaft speed. The large attitude angle indicates the rotational stiffness of the flexure pivot bearings is excessive. The bearings, without pressurization, perform more like a rigid pads bearing rather than true tilting pad bearings.

Figures A.3 through A.6 present the direct and cross-coupled stiffness and damping coefficients for the LOP configuration and for three supply pressure conditions. High supply pressure renders larger direct stiffnesses. The left bearing, having larger clearance, shows smaller direct force coefficients than the right bearing. Note that the force coefficients along the static load direction (X) are similar to those along (Y), i.e. $K_{xx} = K_{yy}$, for the conditions with external feed pressures. However, $K_{yy} > K_{xx}$ for the hydrodynamic case, i.e. without feed pressure. As the supply pressure increases, the direct damping coefficient decreases. The cross-coupled force coefficients are much smaller than the direct force coefficients.

For supply pressures equal to 5.08 bar, 3.72 bar, and 2.36 bar, the force coefficients for the LOP and LBP configurations are nearly identical within the test speed range. On the other hand, the no feed pressure condition renders appreciably different stiffness and damping coefficients for both LOP and LBP configurations. Figure A.7 and A.8 compare the direct and cross-coupled stiffness and damping coefficients for both LOP and LBP configurations. Significant differences are apparent at the lower rotor speeds where the static journal eccentricities are largest. Note that K_{xx} and K_{yy} for LBP are almost the same denoting stiffness symmetry. The direct stiffness for the LBP configuration is close to the loading direction's stiffness (K_{xx}) of the LOP case. The LBP configuration also offers a little larger damping.

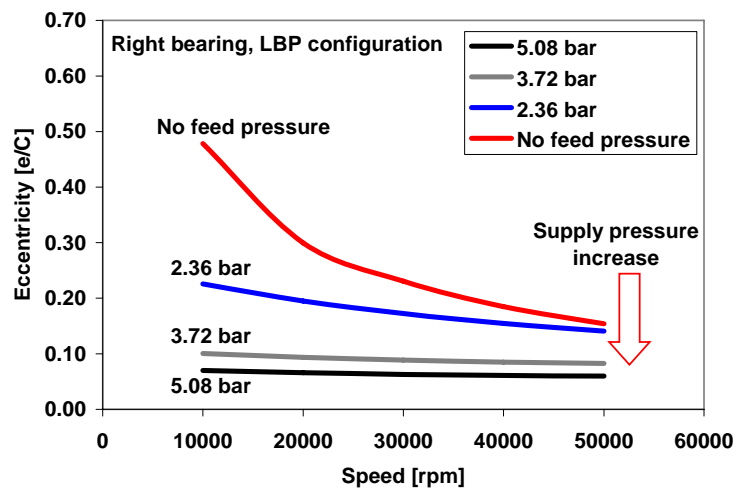
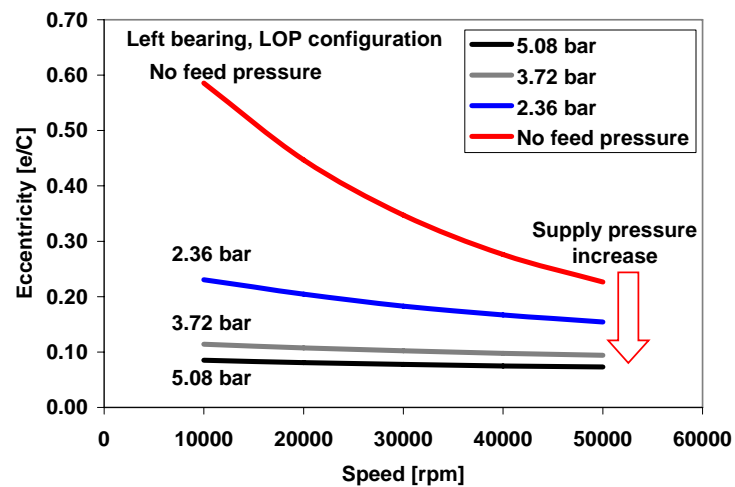
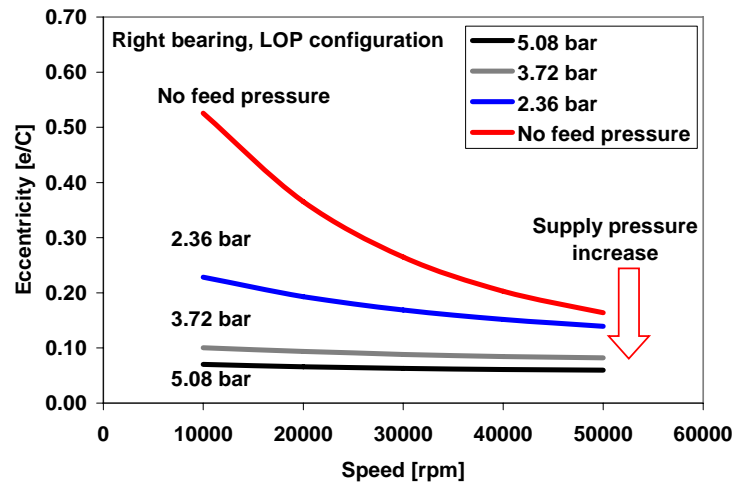
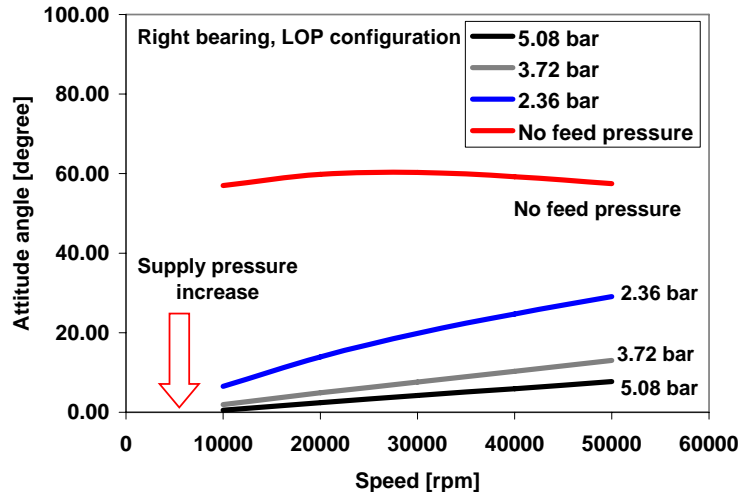
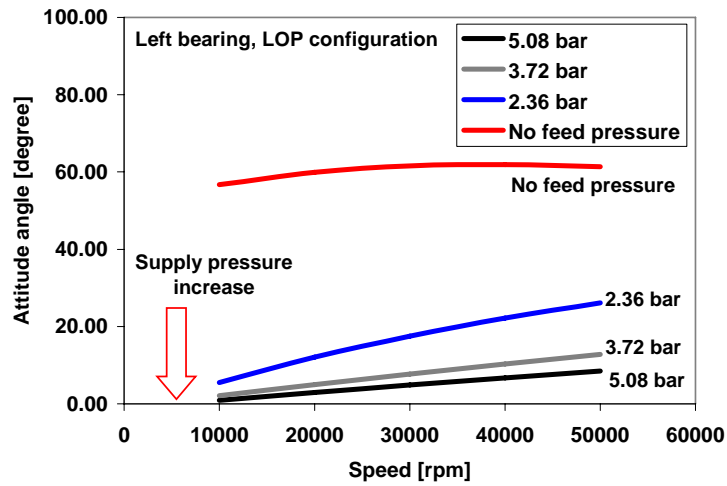


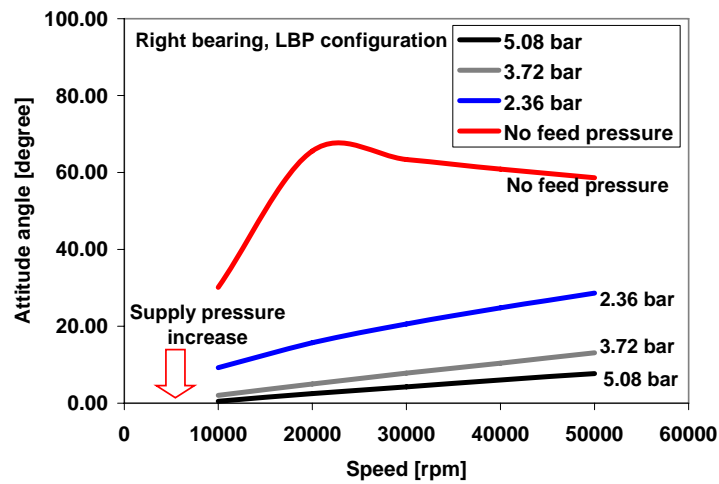
Fig. A.1 Predicted static journal eccentricity (e/C) for increasing feed pressures. LOP and LBP configurations. Static load W=4.04 N



(a) Right bearing, LOP configuration

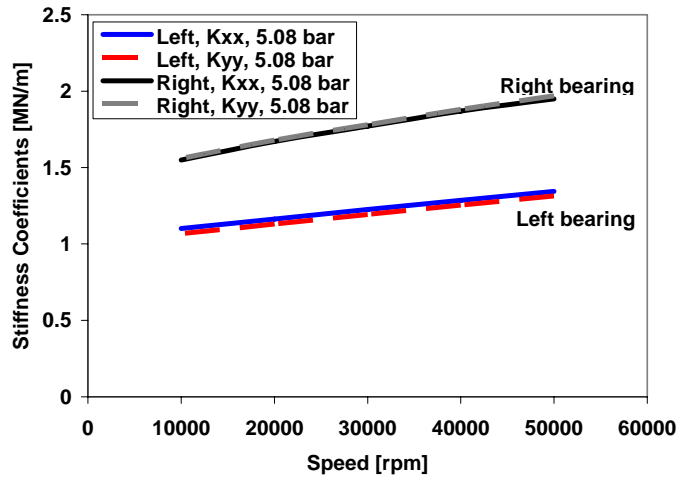


(a) Left bearing, LOP configuration

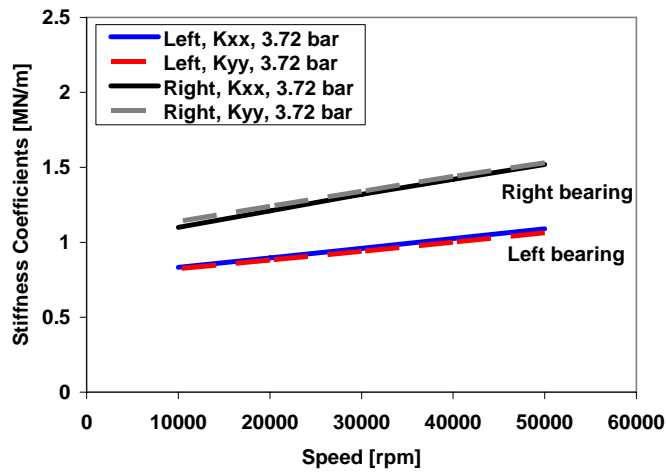


(c) Right bearing, LBP configuration

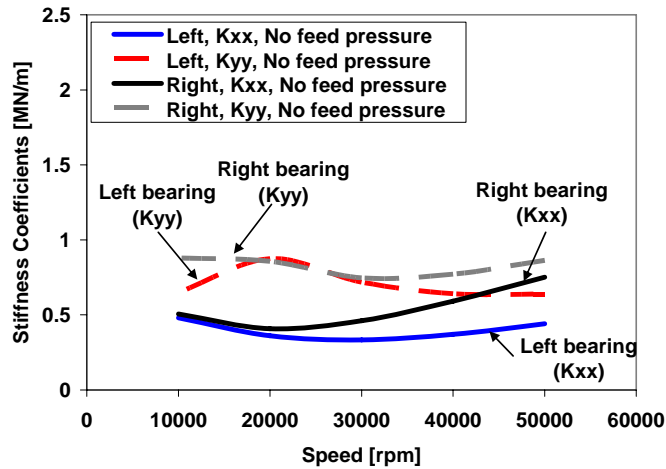
Fig. A.2 Predicted attitude angle for increasing feed pressures. LOP and LBP configuration. Static load $W=4.04$ N



(a) 5.08 bar feed pressure

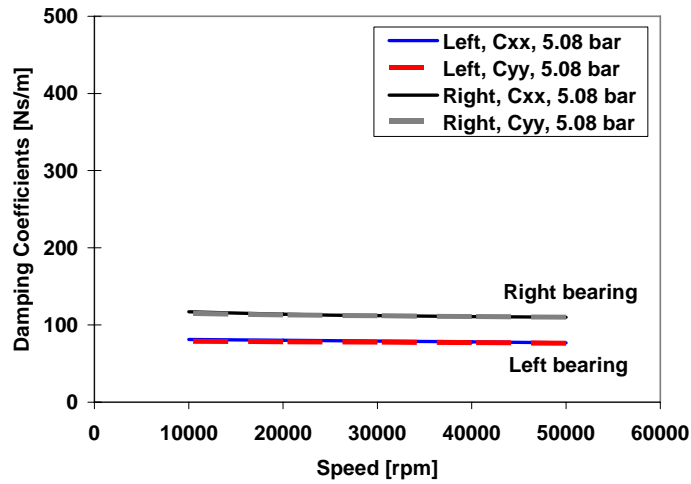


(b) 3.72 bar feed pressure

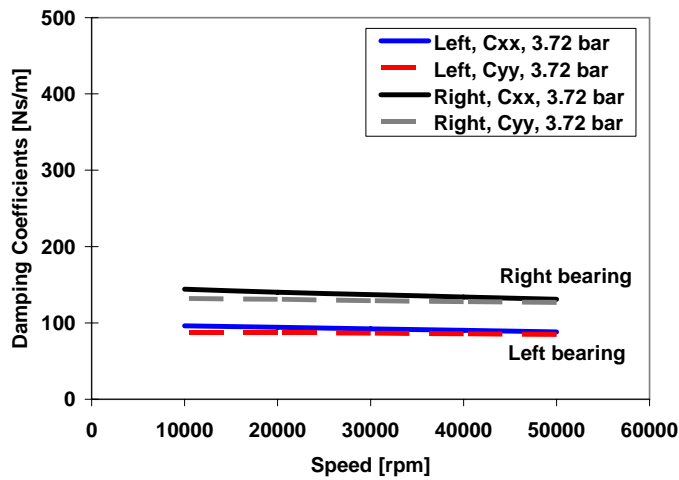


(c) No feed pressure

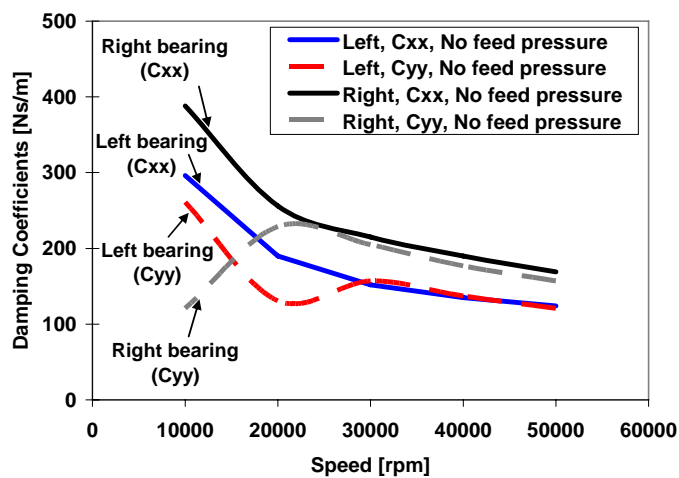
Fig. A.3 Predicted synchronous direct stiffnesses vs. speed. Left and right bearings. LOP configuration. Supply pressures (a) 5.08 bar, (b) 3.72 bar, (c) no feed pressure



(a) 5.08 bar feed pressure

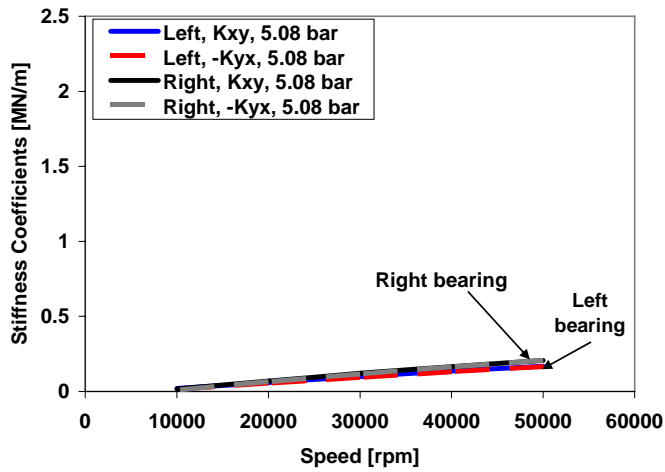


(b) Ps=3.72 bar feed pressure

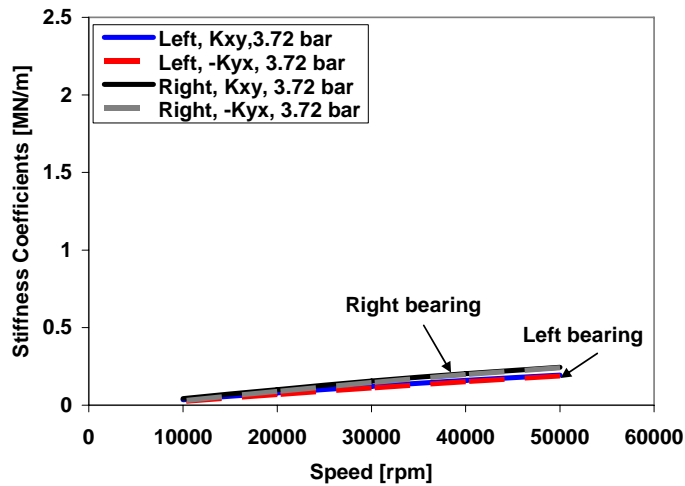


(c) No feed pressure

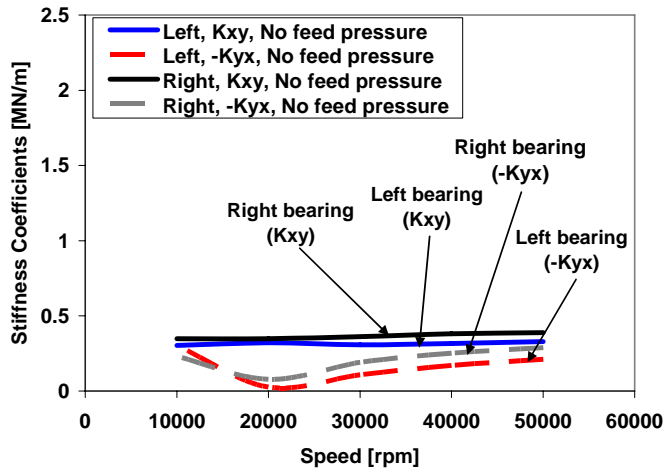
Fig. A.4 Predicted synchronous direct damping coefficients vs. speed. Left and right bearings. LOP configuration. Supply pressures (a) 5.08 bar, (b) 3.72 bar, (c) no feed pressure



(a) 5.08 bar feed pressure

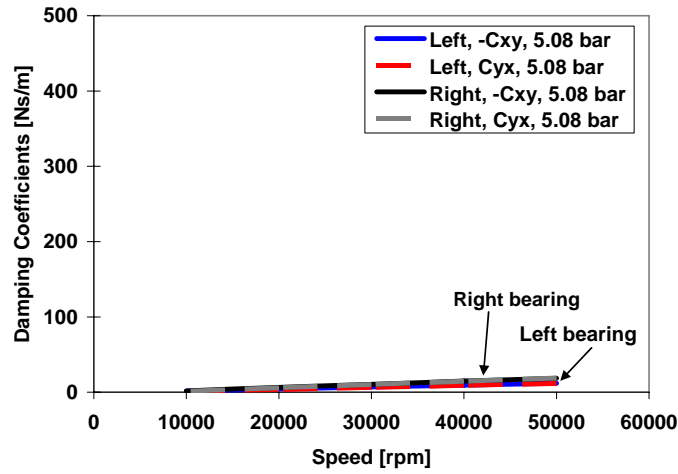


(b) 3.72 bar feed pressure

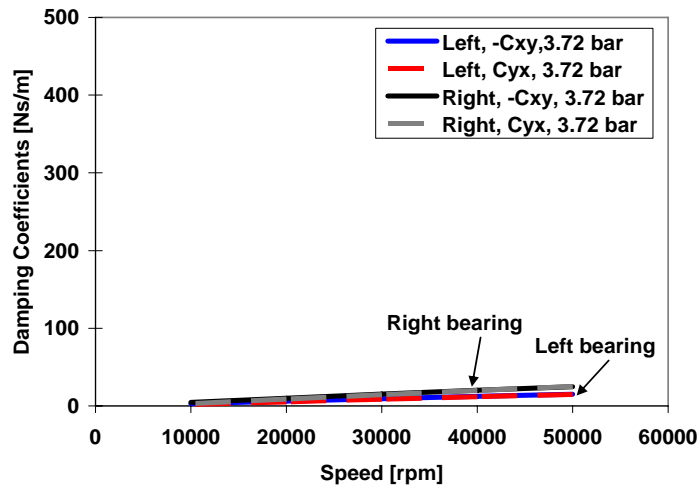


(c) No feed pressure

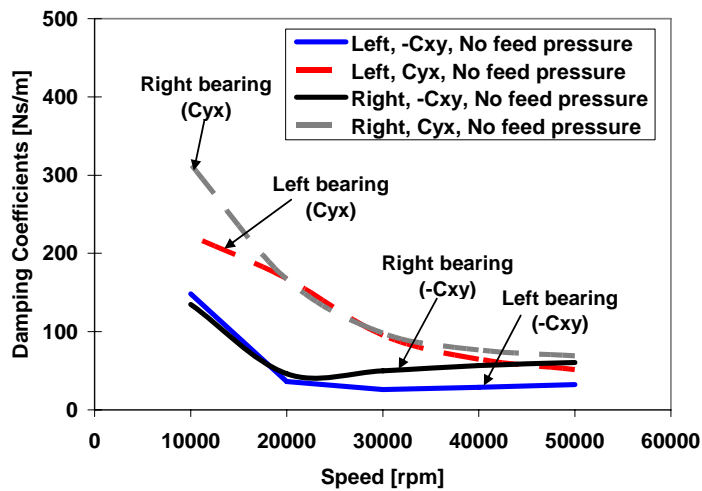
Fig. A.5 Predicted synchronous cross stiffnesses vs. speed. Left and right bearings. LOP configuration. Supply pressures (a) 5.08 bar, (b) 3.72 bar, (c) no feed pressure



(a) 5.08 bar feed pressure

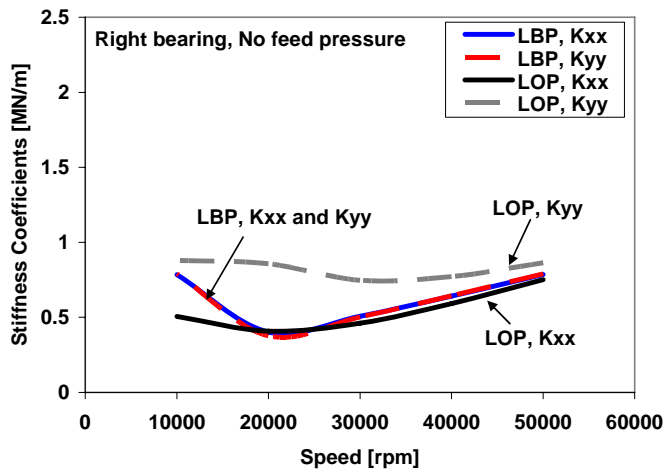


(b) 3.72 bar feed pressure

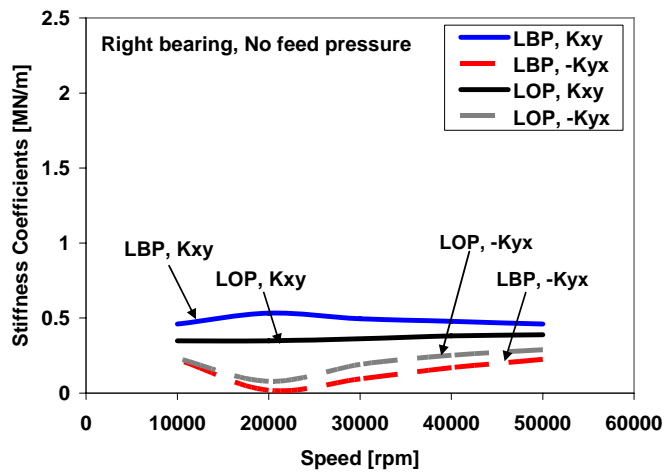


(c) No feed pressure

Fig. A.6 Predicted synchronous cross damping coefficients vs. speed. Left and right bearings. LOP configuration. Supply pressures (a) 5.08 bar, (b) 3.72 bar, (c) no feed pressure

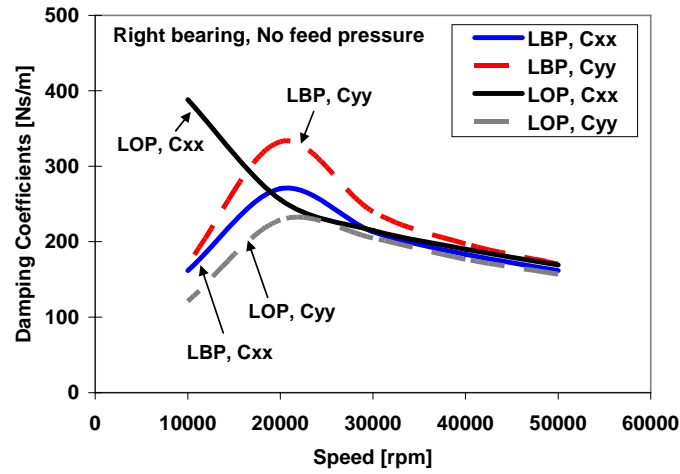


(a) Direct stiffnesses

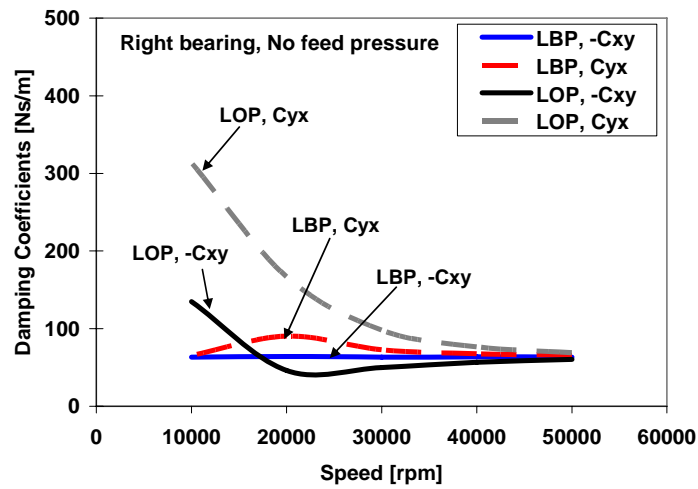


(b) Cross-coupled stiffnesses

Fig. A.7 Comparison of direct and cross-coupled stiffnesses for LOP and LBP configurations. Right bearing without feed pressure. Synchronous speed coefficients



(a) Direct Damping



(b) Cross-coupled Damping

Fig. A.8 Comparison of direct and cross-coupled damping coefficients for **LOP** and **LBP** configurations. Right bearing without feed pressure. Synchronous speed coefficients